Geophysical Journal International

Geophys. J. Int. (2013) **193,** 375–393 doi: 10.1093/gji/ggs117

Generation of slow slip coupled with tremor due to fluid flow along a fault

Teruo Yamashita

Earthquake Research Institute, The University of Tokyo, 1–1-1*, Yayoi, Bunkyo-ku, Tokyo* 113–0032*, Japan. E-mail: tyama@eri.u-tokyo.ac.jp*

Accepted 2012 December 19. Received 2012 December 18; in original form 2012 June 14

SUMMARY

We theoretically study the generation mechanism of slow slip coupled with tremor in a dynamic framework assuming a fault in a fluid-saturated poroelastic medium. Fluid is assumed to flow along the fault, and the fault slip is assumed to create pores on the fault. While the pore creation gives rise to dilatant strengthening, the fluid flow changes the degree of strengthening. Key elements in the modelling are the slip-induced dilatancy rate α_0 and permeability k. Our calculation shows that rupture speeds consistent with observations of slow slip events can be simulated in some ranges of the values of α_0 and k. Our calculation also shows that fault slips stop soon after their onsets if the value of α_0 is large enough. The fluid flow can, however, reactivate frozen slips sporadically because the flow can elevate the fluid pressure. Such slip reactivations can be a model for tremor coupled with slow slip. Reactivated slips are found to migrate backwards through a zone that has already ruptured. We can simulate the backward migration speeds of tremors within a range of 10–150 km hr^{-1} for some values of α_0 and k, which are roughly consistent with recent observations at Cascadia and southwest Japan. The backward migration speeds are generally larger for larger values of k and for smaller values of α_0. If we assume fluid flow in a direction perpendicular to the fault, simulated backward migration speeds are much higher than observed ones.

Key words: Permeability and porosity; Friction; Fault zone rheology; Earthquake dynamics; Subduction zone processes; Fractures and faults.

1 INTRODUCTION

Recent seismological and geodetic observations with dense networks have revealed characteristic phenomena in the interseismic period in some subduction zones, namely, nonvolcanic low-frequency tremors (Obara 2002), slow slip events (SSEs; Dragert *et al.* 2001), low frequency earthquakes (LFEs; Katsumata & Kamiya 2003) and very low frequency earthquakes (VLFs; Ito *et al.* 2007). It is known that tremors often include impulsive body waves, which are categorized as LFEs. It is suggested that SSEs, VLFs and LFEs are relatively slow shear slips on the interface between two plates (Ito *et al.* 2007; Shelly *et al.* 2007). Nonvolcanic tremor often, but apparently not always, accompanies slow slip occurring at plate interfaces at subduction zones (e.g. Obara 2002; Rogers & Dragert 2003; Obara *et al.* 2004; Hirose & Obara 2006). Spatiotemporal change of tremor hypocentres can be an indicator of the expansion of slip zone if the slow slip is coupled with tremor because the slow slip zone agrees with the distribution of tremor hypocentres (Hirose & Obara 2010). Several authors showed that along-strike migration speeds of tremors and SSEs are approximately 10 km d^{-1} ($\sim$10 cm s^{-1}) in a timescale of several days (e.g. Wech *et al.* 2009; Hirose & Obara 2010; Houston *et al.* 2011).

Recent analyses have shown that the tremor migration is more complex. Houston *et al.* (2011) analysed the spatiotemporal change of tremor epicentres in Cascadia and found that tremor can migrate backwards, away from the region where tremor and slip are advancing, through parts of the plate interface that have already ruptured. They showed that these tremor reversals migrate backwards at speeds that are 20–40 times faster than the relatively slow, steady advance of slow slip. Obara *et al.* (2012) also showed the existence of such tremor reversals in southwest Japan; they found migration speeds ranging from 1 to 60 km hr^{-1}. We try to model such feature of tremor together with some other features of SSE in this paper. Although Yamashita & Suzuki (2011), which will be referred to as YS11 below, tried to simulate slow slip coupled with tremor, the backward migration speeds of simulated tremors were all close to the shear wave speed. One of our aims in this paper is to simulate the backward migration speed of tremor on the order of speeds observed by Houston *et al.* (2011) and Obara *et al.* (2012) extending the model developed in YS11.

Several models have been proposed to simulate features of slow slip (e.g. Liu & Rice 2005, 2007; Shibazaki & Shimamoto 2007; Suzuki & Yamashita 2009; Liu & Rubin 2010; Segall *et al.* 2010; YS11; Ando *et al.* 2012). Among them, Suzuki & Yamashita (2009), which is referred to as SY09 below, and YS11 showed that key elements in the simulation of slow slip is the dilatant strengthening and fluid inflow into pores created on the fault; such fluid inflow triggers tremor-like activity (YS11). Liu & Rubin (2010), Segall *et al.*

© The Author 2013. Published by Oxford University Press on behalf of The Royal Astronomical Society.

Downloaded from https://academic.oup.com/gji/article/193/1/375/742358 by guest on 23 April 2024

(2010) and Rubin (2011) also considered the concept of dilatant strengthening for the simulation of slow slip. They, however, did not model the coupling of slow slip with tremor. Some amount of seismic wave energy is radiated by tremor (Rogers & Dragert 2003) and tremors are detectable seismically (e.g. Daub *et al.* 2011), so that dynamic modelling is required to simulate slow slip coupled with tremor. We actually carried out such dynamic analysis in YS11.

Seismological observations of high ratio of P wave speed to S wave speed around tremor sources suggest that metamorphic fluids are present where the tremors occur (Shelly *et al.* 2006; Matsubara *et al.* 2009; Kato *et al.* 2010). Shelly *et al.* (2006) found a zone of high Poisson's ratio near the hypocentres of LFEs, which suggests the existence of fluids and its effect on the generation of LFEs. Remote triggering of LFEs (Miyazawa & Mori 2005) provides evidence for the involvement of high-pressure fluid: note that the rupture threshold is lower for higher fluid pressure according to the Coulomb failure criterion. Slow migration of tremors might be consistent with fluid diffusion (Ito *et al.* 2007; Shelly *et al.* 2007). It may therefore be reasonable to consider the effect of fluid flow in understanding the generation mechanism of slow slip. SY09 and YS11 actually assumed fluid flow in the simulation of slow slip. The fluid was assumed to flow into pores created inelastically on the fault from the surrounding fluid-saturated medium in their studies. They assumed fluid flow only in a direction perpendicular to the fault. The fluid flow will, however, be more complicated near earthquake faults because fault zone permeability is generally anisotropic (e.g. Zhang *et al.* 1999; Faulkner & Rutter 2001; Saffer & Tobin 2011). Zhang *et al.* (1999) measured permeabilities both perpendicular and parallel to an experimental fault with synthetic gouge during slow frictional sliding on the order of 1–10 μm s^{-1}. They showed that significant permeability anisotropy is developed by the fault slip and found that the permeability parallel to the fault is generally larger than that perpendicular to it. Faulkner & Rutter (2001) measured permeabilities of cores taken from the Carboneras fault in southeast Spain. They showed that the permeability is higher three orders of magnitude in a direction parallel to the fault plane than perpendicular to the fault plane. Some seismological observation and gravity measurement also suggest higher permeability in a fault-parallel direction. For example, Miller *et al.* (2004) pointed out, in comparison with calculated fluid pressure change and spatiotemporal variation of hypocentres in the 1997 Umbria-Marche earthquake sequence in central Italy, that sequence of the earthquakes was driven by the migration of high-pressure fluid along the fault. Tanaka *et al.* (2010) showed, by measuring spatiotemporal change of gravity, that the occurrence of long-term slow slip at the plate interface in the Tokai area, Japan, was coupled with the fluid flow along the plate interface.

Taking account of the possibility of higher permeability in a fault-parallel direction, we now consider fluid flow parallel to the fault plane in stark contrast to the treatment in SY09 and YS11, in which fault-normal fluid flow was assumed. It will be shown below that higher rupture speed is simulated when the effect of dilatant strengthening is smaller. Rupture speeds are also higher for larger permeabilities. These results are qualitatively the same as obtained in SY09 and YS11. It will, however, be shown below that we have to assume permeabilities much larger than assumed in SY09 and YS11 to simulate rupture speeds estimated in observations.

We showed in YS11 that simulated tremors are nucleated at slowly extending rupture front and migrate backwards through a zone that has already ruptured; the backward migration speeds of simulated tremors were found to be close to the shear wave speed. In contrast, when the fluid flows in a fault-parallel direction, we can simulate the backward migration speeds of tremors within a range of 10–150 km hr^{-1}. This is roughly consistent with the recent observations of Houston *et al.* (2011) and Obara *et al.* (2012).

2 GOVERNING EQUATIONS

We assume a 2-D antiplane shear fault embedded in a poroelastic medium as in our former papers (Suzuki & Yamashita 2007, 2008, 2010; SY09, YS11). The medium is assumed to be saturated with fluid. The equations governing the spatiotemporal changes in the fluid pressure $\bar{p}_f$ and temperature $\overline{T}_e$ are written in the form (Suzuki & Yamashita 2006, 2010; YS11)

$$\frac{1}{M}\frac{\partial \bar{p}_f}{\partial t} = [(b-\phi_t)\alpha_s + \phi_t\alpha_f]\frac{\partial \bar{T}_e}{\partial t} + \frac{k}{\eta}\nabla^2\bar{p}_f - \frac{\partial \phi_{in}}{\partial t}, \tag{1}$$

$$[(1-\phi_t)\rho_s C_s + \phi_t\rho_f C_f]\frac{\partial \bar{T}_e}{\partial t} = \lambda\nabla^2\bar{T}_e + \dot{Q}\ , \tag{2}$$

where $M = [(b-\phi_t)/K_s + \phi_t/K_f]^{-1}$, $b = 1 - K_v/K_s$, $\phi_t = \phi_e + \phi_{in}$, $\nabla^2 = \partial^2/\partial x^2 + \partial^2/\partial y^2$, k the permeability, C the specific heat, λ the thermal conductivity of the medium, α the thermal expansion coefficient, $\dot{Q}$ the rate of heat generation due to fault slip, ϕ_e the elastic porosity and ϕ_{in} the porosity created inelastically in the shear zone, which is assumed to be located at $-w/2 < y < w/2$. The elastic porosity is assumed to be constant, that is, $\phi_e = 0.1$ as assumed in SY09 and YS11. The definitions of K, G, η and ρ are listed in Table 1. The subscripts s and f denote the solid and fluid phases, respectively. We assume that the fluid pressure is positive for compression and the normal stress is negative for compression. The rate of heat generation $\dot{Q}$ was assumed to be equal to $\sigma_f\Delta\dot{u}/w$ in the shear zone in SY09 and YS11, where σ_f is the sliding frictional stress and $\Delta\dot{u}$ is the slip velocity.

The equation of motion is written as

$$\rho_B\frac{\partial^2}{\partial t^2}(\bar{u}_s)_z = G\nabla^2(\bar{u}_s)_z, \tag{3}$$

where $(\bar{u}_s)_z$ is the z component of the displacement vector and $\rho_B = (1-\phi_t)\rho_s + \phi_t\rho_f$. As stated in Introduction, dynamic modelling is required to simulate tremor, so that the wave eq. (3) is assumed here. We assume the evolution of inelastic porosity in the form

$$\frac{\partial \phi_{in}}{\partial t} = \alpha_0\Delta\dot{u}. \tag{4}$$

as in SY09 and YS11. This equation is obtained if we assume ϕ_{in} much smaller than ϕ_{ss} in eq. (14) of Segall & Rice (1995), where ϕ_{ss} is the steady state value of inelastic porosity. Since we have the

Table 1. Material properties.

Property	Value
Bulk modulus of the solid phase, K_s	3×10^4 MPa
Bulk modulus of the fluid phase, K_f	3.3×10^3 MPa
Drained bulk modulus, K_v	2.4×10^4 MPa
Rigidity, G	1.44×10^4 MPa
Fluid phase viscosity, η	2.82×10^{-4} Pas
Solid phase density, ρ_s	2.7×10^3 kgm^{-3}
Fluid phase density, ρ_f	1×10^3 kgm^{-3}

Note: The bulk modulus of solid phase K_s refers to the intrinsic bulk modulus of the minerals making up the rock and the drained bulk modulus K_v is given by measuring the bulk modulus of the composite solid under the condition of no fluid pressure change.

Downloaded from https://academic.oup.com/gji/article/193/1/375/742358 by guest on 23 April 2024

relation $\phi_{\rm in} \ll 1$ in our simulation as will be shown below, it will be allowed to make the above assumption. Sleep (1997) assumed that the rate of pore production $\partial\phi_{\rm in}/\partial t$ is proportional to the frictional strain rate $\Delta\dot{u}/w$, which is similar to eq. (4) although he assumed the evolution equation in the framework of rate- and state-dependent friction law and the saturation limit for the porosity evolution.

Our calculation will show that the change of inelastic porosity $\phi_{\rm in}$ is negligibly small even in comparison to the elastic porosity $\phi_{\rm e}$, so that we assume the relation $\phi_{\rm t} \simeq \phi_{\rm e}$ in eqs (1)–(3). The drained bulk moduls K_v and permeability k can therefore be assumed to be constant because of this assumption and the assumption of constant elastic porosity.

Fluid seems to flow predominantly in a direction parallel to fault plane at least in some cases as stated in Introduction. We investigate in this paper how the fluid flow in a direction parallel to the fault generates slow slip on this basis. The models assumed in YS11 and in this paper can be regarded as the two end-member models from the viewpoint of fluid flow direction. The permeability is assumed to be significantly high in the shear zone in the present modelling, so that fluid will flow only along the fault. Such fluid flow was actually assumed in the quasistatic simulation of spatiotemporal variation of seismicity by Yamashita (1998, 1999) and others. Mathematical analysis is, however, more difficult when fluid flows along the fault. To simplify the analysis, we neglect the temperature change in the calculation. In other words, we do not consider eq. (2) in this paper. Note that the effect of shear heating is negligible in the range of model parameters for which slow slip is simulated as pointed out by Suzuki & Yamashita (2010) and SY09: we should note that slower fault slip gives rise to lower temperature rise. Since we neglect the temperature change, the simulation is independent of the shear zone thickness w. Hence, we simply assume the fault at $y = 0$ in the modelling, and the fluid is assumed to flow along the plane $y = 0$. We assume the values of model parameters listed in Table 1, which are the same as assumed in YS11.

In the numerical calculation, the fault trace is discretized by a set of equally spaced nodal points ($x_1, x_2, \ldots$) with an interval dx; time is also discretized by a set of equally spaced time steps ($t_1, t_2, \ldots$) with an interval dt. The time evolution of fluid pressure (1) is solved by a finite difference scheme. We actually employ a second-order Adams–Bashforth scheme (e.g. Canuto *et al.* 2006, p. 520): see Appendix A. We employ an efficient boundary integral equation method (BIEM) to solve eq. (3) as in YS11. Our BIEM is highly efficient in comparison to the classical one because of the employment of an asymptotic expression for the kernel function far behind the current time; see Appendix A in YS11 as to the details. We assume the discretization intervals that satisfy the relation $\beta {\rm d}t/{\rm d}x = 0.5$ in all numerical calculations, which gives the best results in our BIEM (Cochard & Madariaga 1994), where $\beta (= 2.386$ km s^{-1}) is the shear wave speed. We assume d$x = 2$ m in all calculations except in calculations in which the effect of the magnitude of dx is examined.

3 FRICTIONAL PROPERTIES ON THE FAULT

We make the same assumptions about frictional properties on the fault and nucleation procedure of rupture as in SY09 and YS11. In other words, we assume the Coulomb law of friction on the fault. The coefficient of friction takes the form of slip-weakening, and it is assumed to decrease linearly from the static frictional coefficient $\mu_{\rm stat}$ to the sliding frictional coefficient $\mu_{\rm slid}$ as the slip undergoes a critical slip-weakening displacement $d_{\rm c}$. The frictional stress is therefore written in the form

$$\begin{aligned} \sigma_{\rm fr} &= \sigma_p - (\sigma_p - \sigma_{\rm f})\Delta u/d_{\rm c} \quad \text{for} \quad 0 < \Delta u \le d_{\rm c} \\ &= \sigma_{\rm f} \qquad\qquad\qquad\qquad\quad \text{for} \quad \Delta u > d_{\rm c}, \end{aligned} \tag{5}$$

where Δu is the slip, $\sigma_{\rm f} = -\mu_{\rm slid}(\sigma_n^0 + p_0 + \bar{p}_{\rm f})$ and $\sigma_p = -\mu_{\rm stat}(\sigma_n^0 + p_0 + \bar{p}_{\rm f})$; σ_n^0 and p_0 are the normal stress and fluid pressure acting on the fault at $t = 0$, respectively. Eq. (5) is assumed as the boundary condition on the fault when eq. (3) is solved. The Coulomb failure criterion is assumed for the analysis of spontaneous rupture growth. In other words, the rupture is assumed to extend when the shear stress $\sigma_{\rm s}$ acting at the rupture front exceeds the failure strength $-\mu_{\rm stat}(\sigma_n^0 + p_0 + \bar{p}_{\rm f})$.

As to the nucleation of rupture, we assume a zone where $\mu_{\rm slid}$ is locally small as in SY09 and YS11; dynamic bilateral rupture propagation is initiated at the centre of the nucleation zone $x = 0$ and its bilateral propagation is artificially forced at 20 per cent of the shear wave speed. The sliding frictional coefficient in the nucleation zone is given by 75 per cent of that assumed outside the nucleation zone. When both rupture tips reach the boundary of the nucleation zone at $|x| = n_i {\rm d}x$, its spontaneous growth is allowed. We assume $n_i = 10$ in all calculations except in calculations in which the effect of nucleation zone size or node-interval size is examined.

As will be shown in Section 5, our present calculation shows that slips stop soon after their onsets when we assume relatively large values for α_0; see also YS11. Such phenomenon occurs because the fluid pressure is reduced abruptly on the fault by the creation of pores. However, the fluid flows into pores with time from the neighbouring fault segments, which tends to raise the fluid pressure there. Such fluid inflow can reactivate frozen slip eventually. As in YS11, we assume in the simulation of slip reactivation that the static friction coefficient $\mu_{\rm stat}$ increases with stationary contact time on the basis of laboratory experiments with rocks (Dieterich 1972). We assume the empirical relation

$$\mu_{\rm stat} = \mu_{\rm stat}^{\rm r} + \gamma \ln(1 + t/\tau) \tag{6}$$

in the calculation, where the healing is assumed to begin at time $t = 0$ and τ is the cut-off time for the time-dependency, which is assumed to be 1 s. Dieterich (1972) pointed out the relation $\mu_{\rm stat}^{\rm r} = \mu_{\rm slid}$ for sandstone and greywacke. However, he also suggested a possibility that $\mu_{\rm stat}^{\rm r}$ is slightly larger than $\mu_{\rm slid}$ for granite and quartzite for normal stress above 40 MPa. We assume a value of $\mu_{\rm stat}^{\rm r}$ slightly larger than that of $\mu_{\rm slid}$ in this paper on the basis of his study. We assume $\gamma = 0.004$ in all calculations below as in YS11, which seems to be a value most appropriate for simulated gouge layer (Paterson & Wong 2005, p. 175).

We assume the critical slip weakening displacement $d_{\rm c} = 0.06$ cm for the earliest slip in each slip sequence; this was also assumed in YS11. We also assume, in the same way as in YS11, that the critical slip-weakening displacement for reactivated slips is negligibly small in comparison to that for the earliest slip in each slip sequence on the basis of theoretical study of Andrews (2004) and data analyses of Fukuyama & Mikumo (2007) and Hirose & Obara (2010). Andrews (2004) showed that slip-weakening displacement is proportional to stress drop in two models assumed by him. We expect that the stress drops for reactivated slips are negligibly small in comparison to that for the earliest slip in each slip sequence because the applied tectonic stress is released by the earliest slip and each reactivated slip merely releases slight stress increase caused by other reactivated slips and the earliest slip. Hence, it will be reasonable to assume much smaller values of critical slip-weakening displacement for

Downloaded from https://academic.oup.com/gji/article/193/1/375/742358 by guest on 23 April 2024

reactivated slips than for the earliest slip as long as we assume the models of Andrews (2004). As stated in YS11, some data analyses also show a tendency that slip-weakening displacements are smaller for smaller-size events. For example, Fukuyama & Mikumo (2007) estimated the slip-weakening displacements, using near-fault data, for the 2000 western Tottori, Japan, earthquake (M_w 6.6) and the 2002 Denali, Alaska, earthquake (M_w 7.9) to be 0.3 and 2.5 m, respectively. Hirose & Obara (2010) estimated cumulative slips associated with short-term SSEs occurring underneath Shikoku, Japan, to be a few cm. This suggests that slip for each LFE is much smaller than a few cm because each short-term SSE includes many LFEs, whose magnitudes are generally smaller than 1.0 (Katsumata & Kamiya 2003), so that the slip-weakening displacement for each LFE should be notably smaller than a few centimetres. The above data analyses therefore imply that slip-weakening displacements are smaller for smaller-size events.

It will therefore be allowed to assume much smaller values of the critical slip-weakening displacement for reactivated slips than for the earliest slip in each slip sequence on the basis of the above studies. Here, we have to take into account that the size of node interval dx must be much smaller than the size of slip-weakening zone for a continuum description of fault slip; the slip-weakening zone is defined as a zone located at the rupture tips where the fault slip is less than the critical slip-weakening displacement d_c. The earliest slip can be simulated in the framework of continuum model on the assumption of d$x = 2$ m: our calculation shows that the slip-weakening zone size for the earliest slip is, at least, larger than three node-intervals. The value d$x = 2$ m will be a minimum allowable value in our calculation considering the computer memory and CPU load. However, if we try to describe reactivated slips assuming a continuum model, we have to assume a value of dx much smaller than 2 m because slip-weakening zone sizes for reactivated slips are much smaller than that for the earliest slip. This is beyond reach with our current computational resources, so that we assume that the critical slip-weakening displacement for reactivated slips is zero in the same way as in YS11. However, this may possibly cause numerical oscillation because the shear stress drops discontinuously at the onset of slip reactivation. To suppress such numerical oscillation, we implement an artificial damping for the slip velocity at every time step as in YS11. If we denote a trial slip velocity at the ith nodal point and mth time step obtained in the absence of damping by $V_{i,m}$ and denote the slip velocity obtained after the application of damping by $V'_{i,m}$, $V'_{i,m}$ can be obtained by solving the simultaneous equations (Yamashita & Fukuyama 1996)

$$V'_{i,m} = V_{i,m} + c(V'_{i+1,m} + V'_{i-1,m} - 2V'_{i,m}), \tag{7}$$

where the parameter c represents the strength of damping. Such artificial damping introduces apparent slip-weakening behaviour for reactivated slips as found in YS11. We assume $c = 0.5$ in all calculations as in YS11. Our assumption on frictional properties implies that slip behaviour of smaller-size events (reactivated slips) is discrete if the damping is not applied. We should note that discrete fault models are not necessarily unrealistic (e.g. Ben-Zion 2008). In fact, Colella *et al.* (2012) and Ben-Zion (2012) assumed inherently discrete models for understanding non-volcanic tremor and slow slip.

The inequalities $-\mu_{slid}(\sigma_n^0 + p_0) < \sigma_s^0 < -\mu_{stat}^0(\sigma_n^0 + p_0)$ should be satisfied for the spontaneous rupture propagation, where σ_s^0 is the initial shear stress acting on the fault and μ_{stat}^0 is the static frictional coefficient at the onset of earliest slip in each simulation of rupture propagation. While the left inequality physically means that positive stress drop is expected at the onset of slip, the right one means that the rupture should not be nucleated spontaneously for $t < 0$. Magnitudes of all three quantities $-\mu_{slid}(\sigma_n^0 + p_0)$, σ_s^0 and $-\mu_{stat}^0(\sigma_n^0 + p_0)$ will be significantly low and there will not be much difference in magnitude between them if the fluid pressure is high enough in the vicinity of faults of slow slips. We assume a sufficiently small value for the initial shear stress σ_s^0 (= 3.5 MPa) as in YS11 on this basis. We also assume the value of $-\mu_{stat}^0(\sigma_n^0 + p_0)/\sigma_s^0$ slightly larger than unity on the basis of the above reasoning, that is, $-\mu_{stat}^0(\sigma_n^0 + p_0)/\sigma_s^0 = 1.045$, which gives $-(\sigma_n^0 + p_0)/\sigma_s^0 = 1.1$ if we assume $\mu_{stat}^0 = 0.95$; see the next paragraph as to the assumption of μ_{stat}^0. The relation $-\mu_{slid}(\sigma_n^0 + p_0) \sim \sigma_s^0$ suggests that the stress drop for slow slip is significantly low. In fact, low stress drop is a remarkable feature of slow slip. Obara (2010) and Schmidt & Gao (2010) actually showed that stress drops of SSEs in southwest Japan and in Cascadia range from 0.01 to 0.1 MPa, which are much smaller than those for ordinary earthquakes.

It was shown in YS11 that the rupture speed is lower for larger values of μ_{stat}^0 when the values of $-(\sigma_n^0 + p_0)/\sigma_s^0$ and $\mu_{stat}^0 - \mu_{slid}$ are fixed. In this paper, we assume on the basis of the above finding sufficiently large values for the static and sliding frictional coefficients, that is, $\mu_{stat}^0 = 0.95$ and $\mu_{slid} = 0.85$ in all calculations below. We also assume $\mu_{stat}^r = 0.851$, which is slightly larger than μ_{slid} . Classical laboratory measurements show that static frictional coefficient is in the range 0.6–0.85, independent of lithology (Byerlee 1978) although it is unknown what value static frictional coefficient actually takes at locations where SSEs occur. Although our assumption of μ_{stat}^0 is somewhat larger than classical values, we have to note that the same rupture speed can be simulated by assuming smaller values for μ_{stat}^0 if we assume larger values for $-(\sigma_n^0 + p_0)/\sigma_s^0$: see fig. 13 in YS11.

Spatial distributions of all the model parameters are assumed to be homogeneous outside the nucleation zone in all calculations below. In such an approach, we may be able to understand how system dynamics itself affects the generation of slow slip; our aim here is not the quantitative but fundamental understanding of the phenomena. To develop a quantitative understanding, we may have to take account of spatial heterogeneity or anisotropy in the distribution of model parameters (e.g. Ando *et al.* 2012).

4 RUPTURE GROWTH AND MOMENT EVOLUTION

We now investigate how macroscopic-scale rupture behaviour depends on the values of α_0 and k. These values are rather arbitrarily assumed so as to simulate rupture speeds consistent with observations of SSEs. We now consider the rupture growth and moment evolution as examples of the macroscopic-scale rupture behaviour. As long as these macroscopic-scale rupture phenomena are concerned, our calculation shows that there is little dependence on the discretization and assumed size of nucleation zone (Appendix B); the application of damping does not affect these phenomena as will be exemplified in Section 5.

Fig. 1 shows the dependence of the rupture growth curve on the values of α_0 and k. We find in Fig. 1 that the rupture speed is higher for larger values of k and for smaller values of α_0. This occurs because fluid pressure is elevated more rapidly for larger values of k and for smaller values of α_0 as observed in YS11. Larger amount of computer memory is required for such cases because of higher rupture speeds. Hence the computation is stopped earlier for smaller values of α_0 in Fig. 1(b).

Downloaded from https://academic.oup.com/gji/article/193/1/375/742358 by guest on 23 April 2024

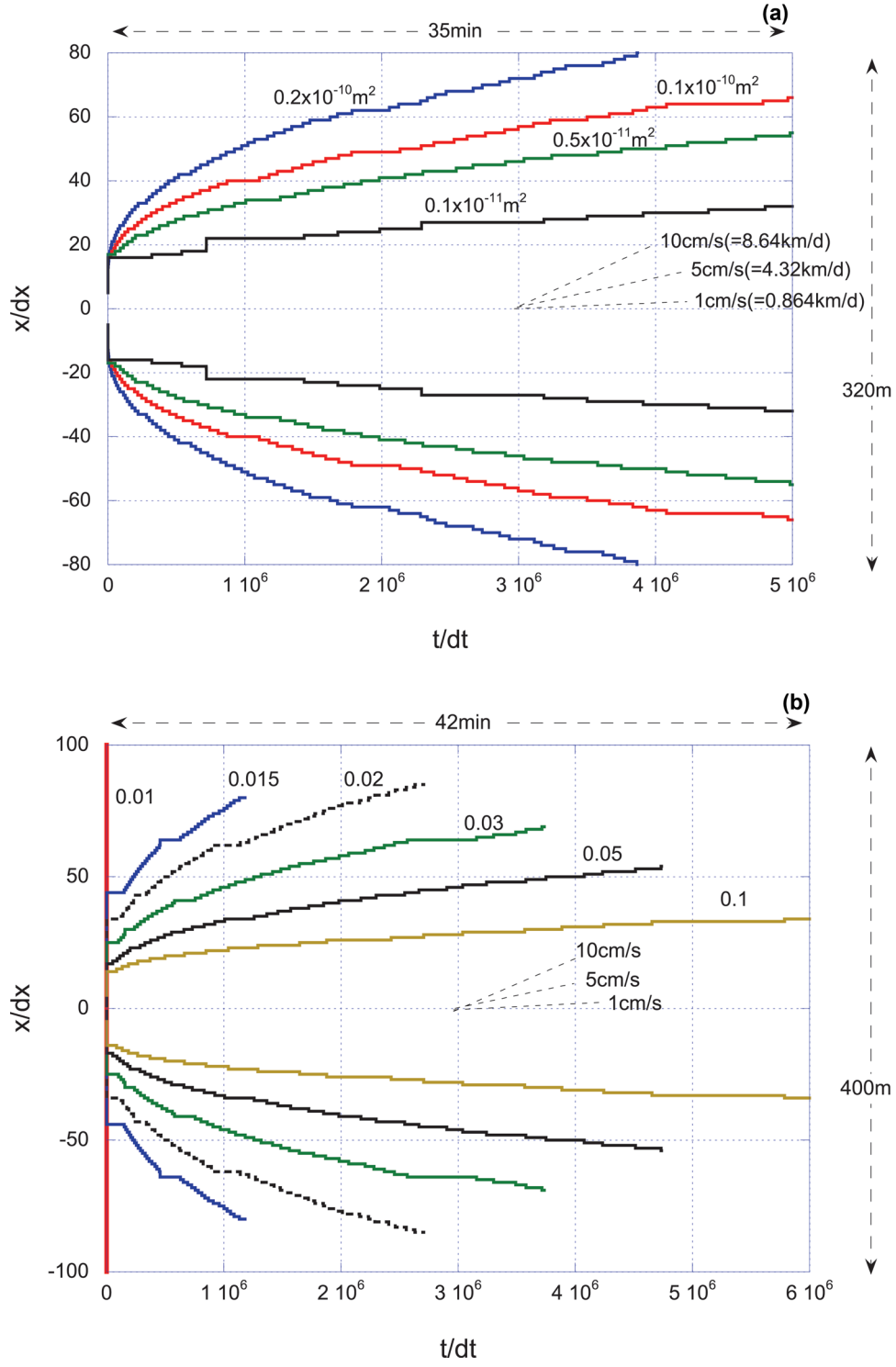

Figure 1. Dependence of rupture growth on the values of k and α_0. The values of α_0 and k are fixed at 0.05 and 0.5×10^{-11} m^2 in (a) and (b), respectively. The curve parameters in (a) and (b) are the values of k and α_0, respectively. The nondimensional time $t/\mathrm{d}t = 5 \times 10^6$ is approximately equal to $t = 35$ min. The non-dimensional length $x/\mathrm{d}x = 100$ corresponds to $x = 200$ m. Calculations are stopped earlier during the rupture growth for smaller values of α_0 in (b) because of the capacity of computer. Broken line segments show the scale for the rupture speed.

What should be noted in Fig. 1 is that rupture speeds consistent with observations of SSEs on the order of 10 km d^{-1} (e.g. Wech *et al.* 2009; Hirose & Obara 2010) occur only for permeabilities greater than $k = 0.2 \times 10^{-10}$m^2 for $\alpha_0 = 0.05$ (Fig. 1a). We can assume smaller values for k to simulate the same rupture speed if smaller values are assumed for α_0. For example, if we assume $k = 0.5 \times 10^{-11}$m^2 and $\alpha_0 = 0.02$, the rupture speed on the order of 10 km d^{-1} can be simulated at least during our computation (Fig. 1b). However, if we assume values of α_0 smaller than a certain threshold, rupture growth is accelerated soon after the nucleation

Downloaded from https://academic.oup.com/gji/article/193/1/375/742358 by guest on 23 April 2024

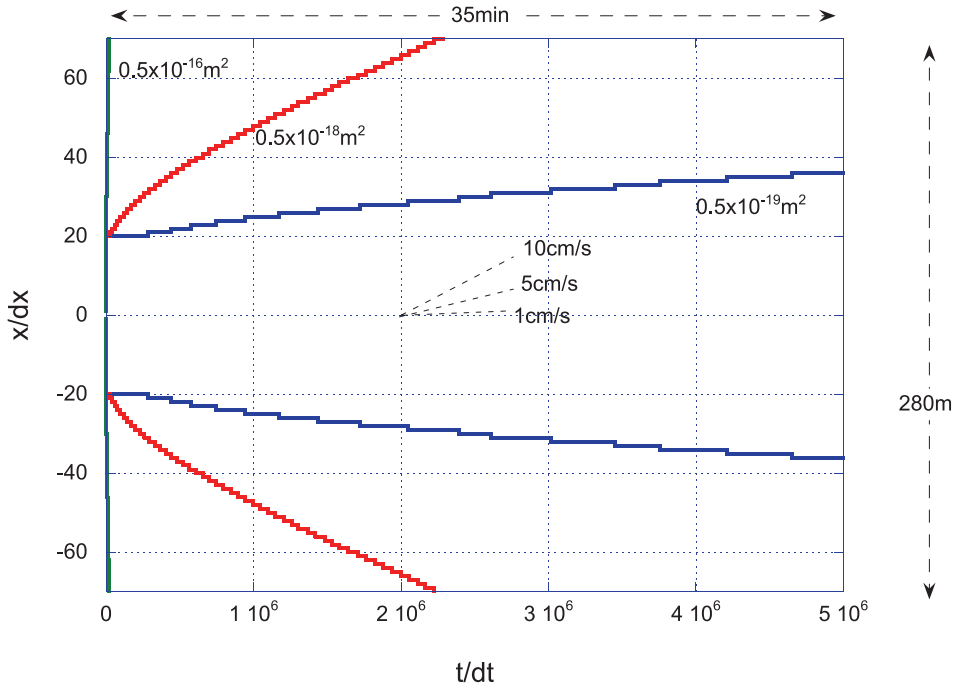

Figure 2. Simulated rupture growth for the model in which the fluid flows only in a direction perpendicular to the fault. The curve parameters are the values of k; the value of α_0 is fixed at 0.05. Broken line segments show the scale for the rupture speed.

and the rupture speed becomes close to the shear wave speed for any values of k; for example, our calculations show that the rupture speeds are close to the shear wave speed for all examples with $k = 10^{-14}$, $= 10^{-17}$ and $= 10^{-20}\text{m}^2$ when α_0 is fixed at 0.01. This suggests that the threshold of α_0 for the simulation of slow slip lies between $\alpha_0 = 0.01$ and $= 0.02$. Since the slow rupture growth consistent with observations of SSEs can be simulated with the permeability $k \sim 0.5 \times 10^{-11}\text{m}^2$ when $\alpha_0 = 0.02$ (Fig. 1b), it will be improbable to simulate SSEs, in the framework of our model, with permeabilities 10^{-21} to 10^{-13} m^2, which are generally supposed as permeabilities of exhumed faults (e.g. Faulkner & Rutter 2001; Wibberley & Shimamoto 2003).

When fluid flows in a direction perpendicular to the fault, slow sustained rupture growth consistent with observations of SSEs occurs for much smaller values of permeability than assumed in this paper as found in YS11. Illustrative examples are shown in Fig. 2; the calculation is done using the method developed in YS11. Fig. 2 shows that rupture speed consistent with observations of SSEs occurs for permeability $k = 0.5 \times 10^{-18}\text{m}^2$ for $\alpha_0 = 0.05$. Although it is not very straightforward to understand why we have to assume vastly different permeabilities in the two fluid-flow models to simulate the slow rupture growth consistent with observations, Fig. 3 suggests that the difference in the length scale over which significant fluid flow occurs makes such a difference in the permeability. Let us shortly study how the difference in the fluid-flow length scale affects the permeability required in the two models. We now ignore the history of rupture growth to simplify the analysis. Under such assumption, the fluid-flow length scale will approximately be given by the shear zone thickness in the model of fault-normal fluid flow: fluid flows predominantly across this zone because of the creation of pores there, which triggers the fluid inflow. The fluid-flow length scale will be on the order of rupture zone size (Fig. 3) in the model of fault-parallel fluid flow if the rupture growth history is ignored because pores are created over the rupture zone (Fig. 4). Let us now compare the rupture growth curve

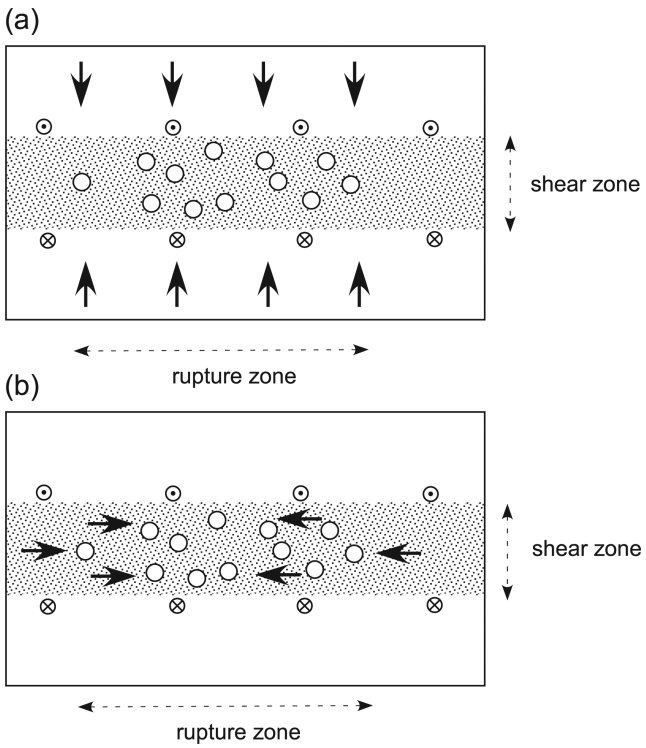

Figure 3. Schematic illustration of fluid flow induced by the pore creation in the models of (a) fault-normal and (b) fault-parallel fluid flows. The open circles in the shear zone schematically illustrate the inelastically created pores and the arrows represent the direction of fluid flow.

with the permeability $k = 0.2 \times 10^{-10}\text{m}^2$ in Fig. 1(a) and one with $k = 0.5 \times 10^{-18}\text{m}^2$ in Fig. 2 employing the concept of fluid-flow length scale defined above. Note that the rupture speed is almost equal in the above two examples and is approximately equal to

Downloaded from https://academic.oup.com/gji/article/193/1/375/742358 by guest on 23 April 2024

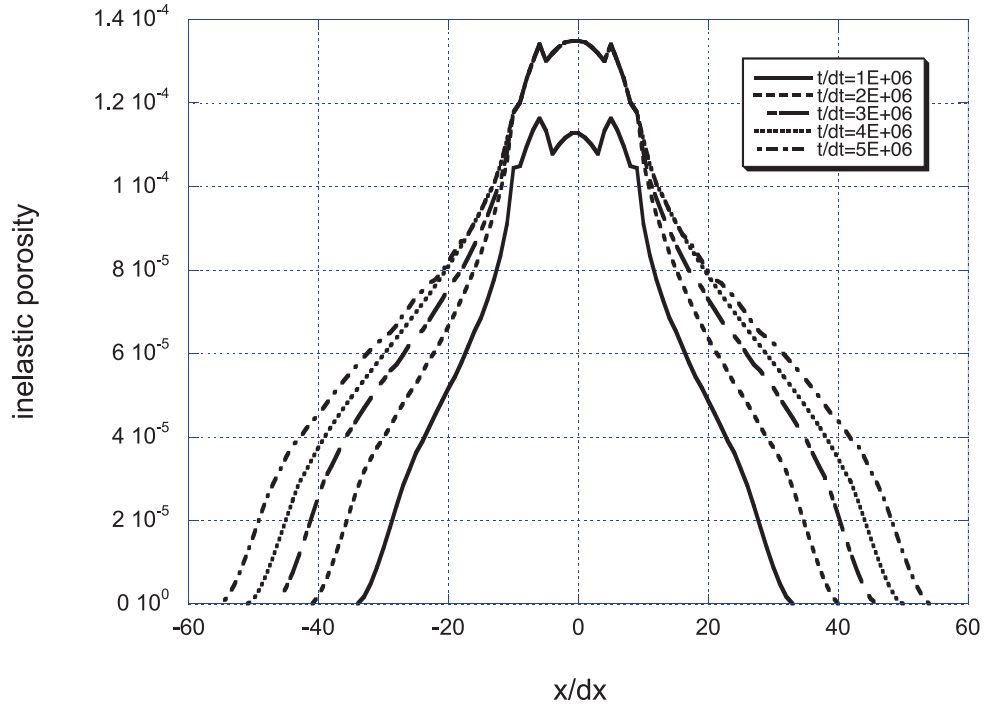

Figure 4. Change of inelastic porosity on the fault for the case with $\alpha_0 = 0.05$ and $k = 0.5\times10^{-11}$ m^2. As mentioned in Section 2, the inelastic porosity change simulated in the calculation is negligibly small in comparison to the elastic porosity. Such negligible change in inelastic porosity can affect the fluid pressure change because the term $\partial\phi_{in}/\partial t$ in eq. (1) is not negligible in comparison to the other terms.

5–10 cm s^{-1} at $t/\mathrm{d}t \sim 3 \times 10^6$; the rupture zone size is about 300 m in the two examples at this instant. The ratio of the fluid-flow length scale for the fluid-normal fluid flow to that for the fault-parallel fluid flow will therefore be on the order of 5 cm/300 m $= 1.7 \times 10^{-4}$ at time step $t/\mathrm{d}t \sim 3 \times 10^6$. We will be able to equate the fluid-flow length scale defined above to the fluid diffusion distance defined as $\sqrt{Mkt/\eta}$ at least approximately. The ratio of the fluid diffusion distance for the above two examples will therefore be given by the square root of the permeability ratio, that is, $\sqrt{0.5\times10^{-18}/0.2\times10^{-10}}=1.6\times10^{-4}$ when time t is fixed. This is of the same order of magnitude as that of the fluid-flow length scale ratio obtained above. The above consideration therefore suggests that the difference in the fluid-flow length scale makes a difference in the value of permeability required to simulate the same slow rupture speed between the fault-normal and fault-parallel fluid flow models. We made a highly rough estimate in the above consideration. For example, if we take account of the rupture growth history, the fluid-flow length scale and fluid diffusion distance may vary with location on the rupture zone. However, the above consideration may give an insight into why we have to assume significantly different permeabilities in the two fluid-flow models to simulate the slow rupture growth consistent with observations.

Fig. 5 shows the dependence of the temporal change of cumulative moment release M_0 on the values of α_0 and k. We find here that the cumulative moment release is much slower than expected from the relation $M_0(t) \sim t^2$, which is the solution for dynamically propagating classical singular crack (e.g. Kostrov 1964). Such behaviour was also simulated in YS11.

In summary, macroscopic-scale rupture behaviour simulated in this paper is qualitatively the same as simulated in YS11 except that much larger permeabilities must be assumed in this paper to simulate the same slow rupture speed.

5 SIMULATION OF TREMOR COUPLED WITH SLOW SLIP

5.1 Features of reactivated slips

We found in YS11 that frozen slips are reactivated sporadically because fluid inflow from the surrounding fluid-saturated medium elevates the fluid pressure on the fault. Such sporadic slip reactivation was regarded as a model for non-volcanic tremor in YS11. We also find in this paper that the fluid flow along the fault can reactivate frozen slips.Fig. 6 shows an example of spatiotemporal evolution of slip velocity during the rupture propagation. We assume $\alpha_0 = 0.05$ and $k = 0.5 \times 10^{-11}$m^2 here as well as in many examples of calculation in this paper because relatively long calculation can be carried out for these values without much load to the computer, and simulated rupture speed is not much different from observed for SSEs (Fig. 1a). Fig. 6 shows a large number of slip reactivations during the rupture propagation. Such sporadic reactivations of slips can be a model for non-volcanic tremor coupled with slow slip because reactivated slips have relatively large slip velocities as will be shown below.

As exemplified in Fig. 6, our calculation shows that slip reactivations begin at the extending rupture front where the slip velocity is localized, and that reactivated slips migrate backwards to a zone that has already ruptured. Slip velocity localization at the extending rupture front occurs because of intense dilatant strengthening; the strengthening is more intensive for larger values of α_0 as found in YS11. Examples of individual slip reactivations are illustrated in Fig. 7. Backward migration speeds are estimated by a linear least-squares method in this paper. As exemplified in Fig. 7, slip velocities of reactivated events are much larger than that of slip localized near the front of slow slip region. Fig. 7 actually shows that the peak values of non-dimensional slip velocities of reactivated slips are about

Downloaded from https://academic.oup.com/gji/article/193/1/375/742358 by guest on 23 April 2024

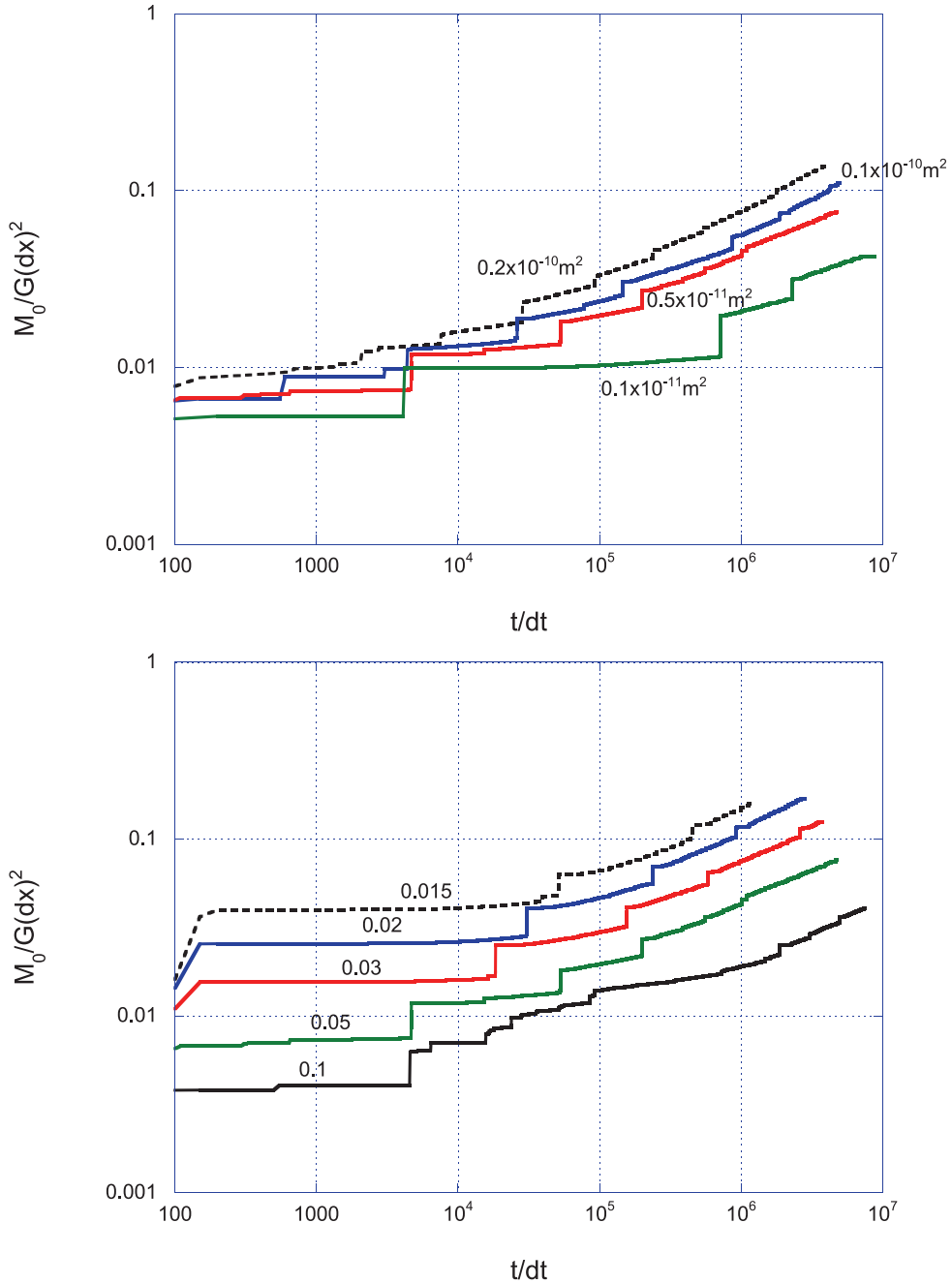

Figure 5. Dependence of moment evolution on the values of k and α_0. The values of α_0 and k are fixed at 0.05 and 0.5×10^{-11} m^2 in (a) and (b), respectively. The curve parameters in (a) and (b) are the values of k and α_0, respectively. Irregular changes are due to slip reactivations.

$6.0 \times 10^{-6} \sim 7.0 \times 10^{-6}$ at $t/\mathrm{d}t = 3.0 \times 10^6 \sim 4.0 \times 10^6$ (Fig. 7). These values correspond to slip velocities 1.4–1.7 cm s^{-1}, which will be detectable seismically (Daub *et al.* 2011). Reactivated slips will therefore be regarded as a model for non-volcanic tremor. By contrast, our calculation shows that the peak value of non-dimensional slip velocity near the front of slow slip region is about 5.0×10^{-10} in the range $t/\mathrm{d}t = 3.0 \times 10^6$ to 4.0×10^6. This corresponds to slip velocity 1.2×10^{-4}cm s^{-1}, which is one order larger in magnitude than the average slip velocity of SSEs (around 1.0×10^{-5}cm s^{-1}; Hirose & Obara 2005).

As mentioned before, we rather arbitrarily assume values of α_0 and k that can simulate rupture speeds consistent with observations of SSEs (Fig. 1). The slip reactivation never turns the growth of slow slip region seismic for these values of α_0 and k. Although stress perturbation due to slip reactivation may slightly advance the slow slip region, it cannot trigger unstable growth because of rapid increase in slip resistance with increasing slip for values of α_0 assumed for the simulation of slow slip. This is also understandable from the behaviour of the transition from rupture nucleation to spontaneous rupture growth observed in our simulation; see Figs 1 and 6. We assume dynamic rupture nucleation in each simulation. However, as soon as the rupture front comes out of the nucleation zone, the growth is strongly decelerated and rupture speeds roughly consistent with observations of SSEs can be observed. This exemplifies

Downloaded from https://academic.oup.com/gji/article/193/1/375/742358 by guest on 23 April 2024

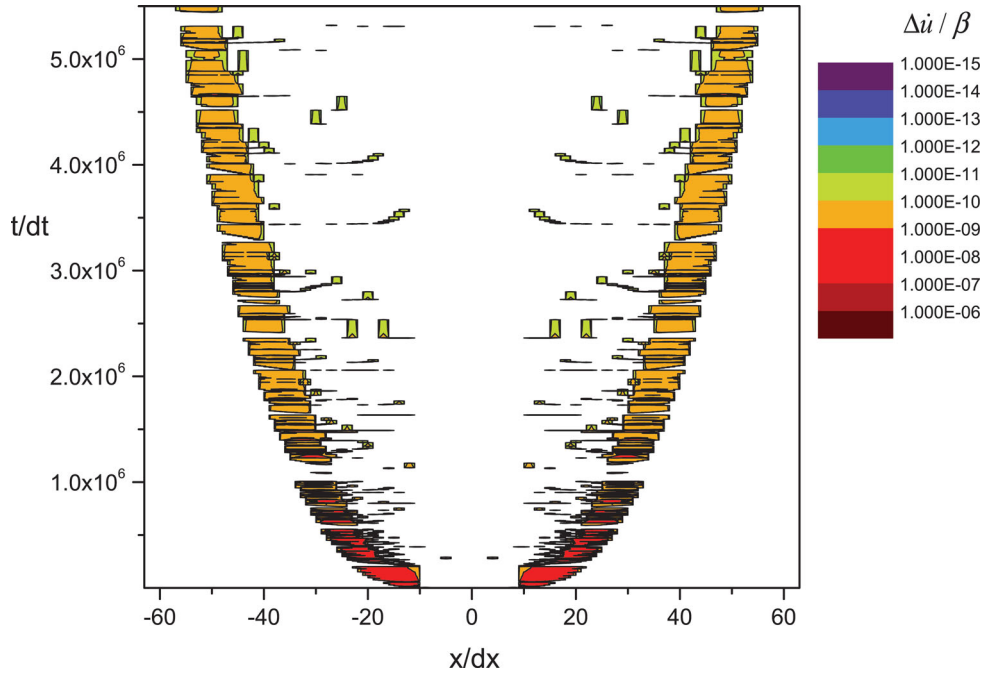

Figure 6. Spatiotemporal change of slip velocity during the rupture growth. We assume $\alpha_0 = 0.05$ and $k = 0.5 \times 10^{-11}$ m^2 in the calculation. The slip velocity is plotted every 100 time steps, so that continuous migration of reactivated slip sometimes appears to be discontinuous when its migration speed is sufficiently high; such slips are missing in the illustration when the migration distance is small enough. The nondimensioal slip velocity $\Delta\dot{u}/\beta = 1.0\mathrm{E} - 10$ corresponds to the slip velocity 2.4×10^{-5} cm s^{-1}.

that dynamic perturbation due to slip reactivation does not trigger unstable growth of slow slip region.

Although the backward migration of reactivated slip was also simulated in YS11, backward migration speeds of reactivated slips simulated here are much lower than those simulated in YS11. For comparison, an example of spatiotemporal change of slip velocity is shown in Fig. 8 for the fault-normal fluid flow model assumed in SY09 and YS11; $\alpha_0 = 0.05$ and $k = 0.5 \times 10^{-18}$m^2 are assumed in the calculation. Backward migration speeds of reactivated slips are much higher in Fig. 8 than in Fig. 6. Our calculation for the fault-normal fluid flow model actually shows that backward migration speeds of all reactivated slips are close to the shear wave speed; see also YS11 as to the details. Such difference in the backward migration speeds may occur at least partly because the fluid pressure elevation is more homogeneous over the rupture zone in the fault-normal fluid flow model than in the fault-parallel fluid flow model (Fig. 3). Note that fluid flows into a fault segment efficiently only when some slip-induced dilatancy occurs in the neighbouring fault segments in the fault-parallel fluid flow model. By contrast, fluid flows into a fault segment irrespective of the behaviour of neighbouring fault segments in the fault-normal fluid flow model. Such difference in the fluid flow behaviour will give rise to more heterogeneous fluid pressure distribution in the fault-parallel fluid flow model. Extension of slow slip region will be more irregular in Fig. 6 than in Fig. 8 because the fluid pressure distribution is more heterogeneous in the fault-parallel fluid flow model.

5.2 Reactivated slip as mesoscopic-scale rupture phenomenon

As exemplified in Fig. 6, the slip reactivation is regarded as relatively localized phenomenon, so that it may be referred to as a mesoscopic-scale rupture phenomenon. This implies that slip reactivation depends more on applied damping or the assumed size of node interval than the macroscopic-scale rupture phenomena. The introduction of damping generally causes a smoothing effect, so that smaller events may possibly be more affected by the damping. However, our calculation shows that the introduction of damping gives negligible effect on the propagation of reactivated slip at least for relatively large-size events; compare Fig. 9 with Fig. 6. Fig. 9 also indicates that large-scale numerical instability does not occur even if we assume zero damping.

We next examine how the assumed size of node-interval affects the slip reactivation. If we assume the same nucleation zone size as assumed in Fig. 6 and make the calculation for the same time steps, the required computer memory and computation time will be much larger for smaller values of dx. We therefore fix the value of n_i at 10 here; the nucleation zone is located at $-n_i \mathrm{d}x \leq x \leq n_i \mathrm{d}x$ as stated before. This means that the nucleation zone size is smaller for smaller values of dx. Our calculation shows that rupture speed, which is regarded as a macroscopic-scale rupture phenomenon, is almost independent of the nucleation-zone size as well as the size of node interval (Fig. 10; see also Appendix B). However, the location and time of nucleation of slip reactivation depends on the assumed size of node interval: compare Fig. 6 with Fig. 11. This may be because slip reactivation, which is regarded as a mesoscopic-scale rupture phenomenon, depends more on the discretization than the macroscopic-scale ones. Although the artificial damping somewhat suppresses the dependence on the size of node interval, intense nonlinear interactions between the fluid pressure change and fault slip gives rise to some dependence. In other words, a slight change in the occurrence time of slip reactivation early in a rupture growth process affects later slip reactivation significantly. Our main concern is, however, about the backward migration speed of reactivated slip, so that we focus on how the backward migration speed depends on the discretization in the next subsection.

Downloaded from https://academic.oup.com/gji/article/193/1/375/742358 by guest on 23 April 2024

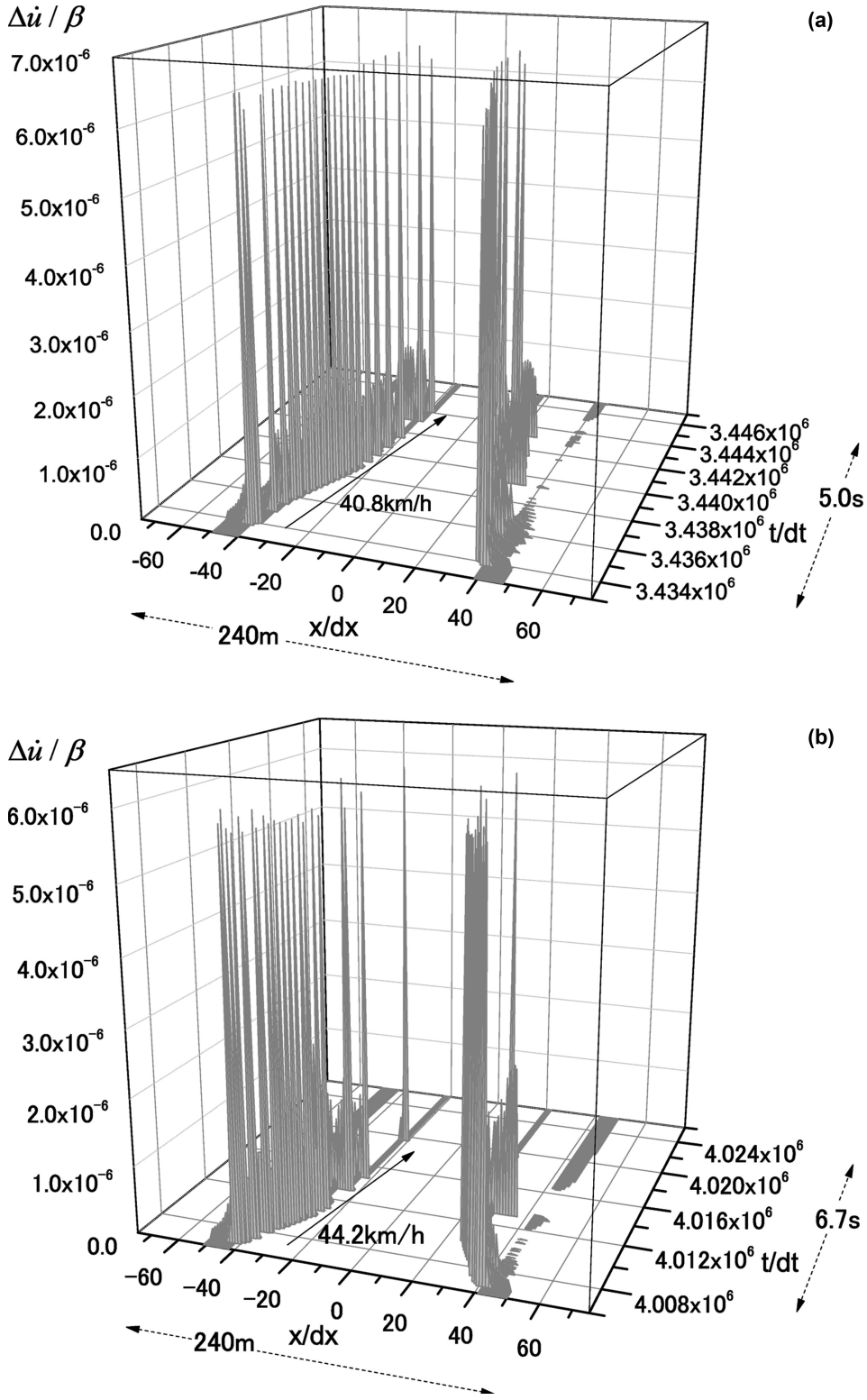

Figure 7. Two examples of reactivated slips, illustrated in Fig. 6, which are nucleated at the front of slow slip region and migrate backwards with speeds much slower than the shear wave speed. We observe that slip velocities of reactivated events are several orders larger in magnitude than the velocity of slip localized near the front of slow slip region.

5.3 Slow backward migration of reactivated slip

Fig. 12 shows the backward migration speeds of reactivated slips for four cases in which d$x = 1$, 1.25, 1.5 and 2 m are assumed; $\alpha_0 = 0.05$ and $k = 0.5 \times 10^{-11}\mathrm{m}^2$ are assumed in all calculations here. We assume $n_i = 10$ in all the four cases except in the case with d$x = 1$ m; we assume both $n_i = 10$ and 20 in the case with d$x = 1$ m, so that the nucleation zone size is the same for the two cases (d$x = 1$ m, $n_i = 20$) and (d$x = 2$ m, $n_i = 10$). Note that we assumed d$x = 2$ m and $n_i = 10$ in all calculations up to Fig. 9. In

Downloaded from https://academic.oup.com/gji/article/193/1/375/742358 by guest on 23 April 2024

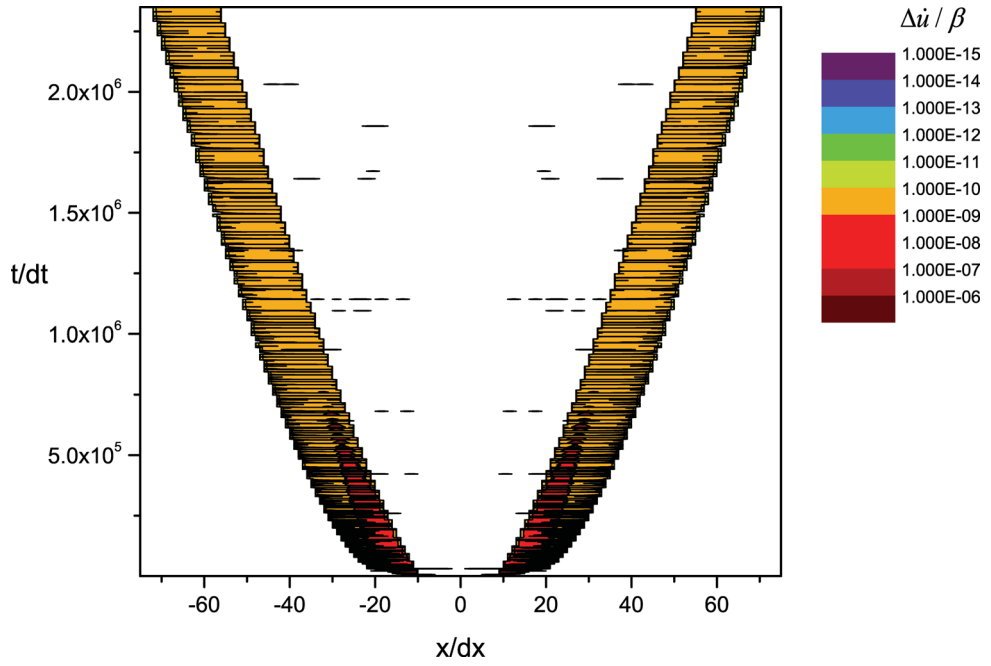

Figure 8. Spatiotemporal change of slip velocity during the rupture growth; fluid is assumed to flow in a direction perpendicular to the fault. The slip velocity is plotted every 100 time steps. We assume $\alpha_0 = 0.05$ and $k = 0.5 \times 10^{-18}$ m^2 in the calculation. Our calculation shows that all reactivated slips propagate backwards almost parallel to the x-axis with a speed close to the shear wave speed. Continuous migrations of reactivated slips sometimes appear to be discontinuous because of the plotting every 100 time steps; some slips are even missing in the illustration when the migration distance is small.

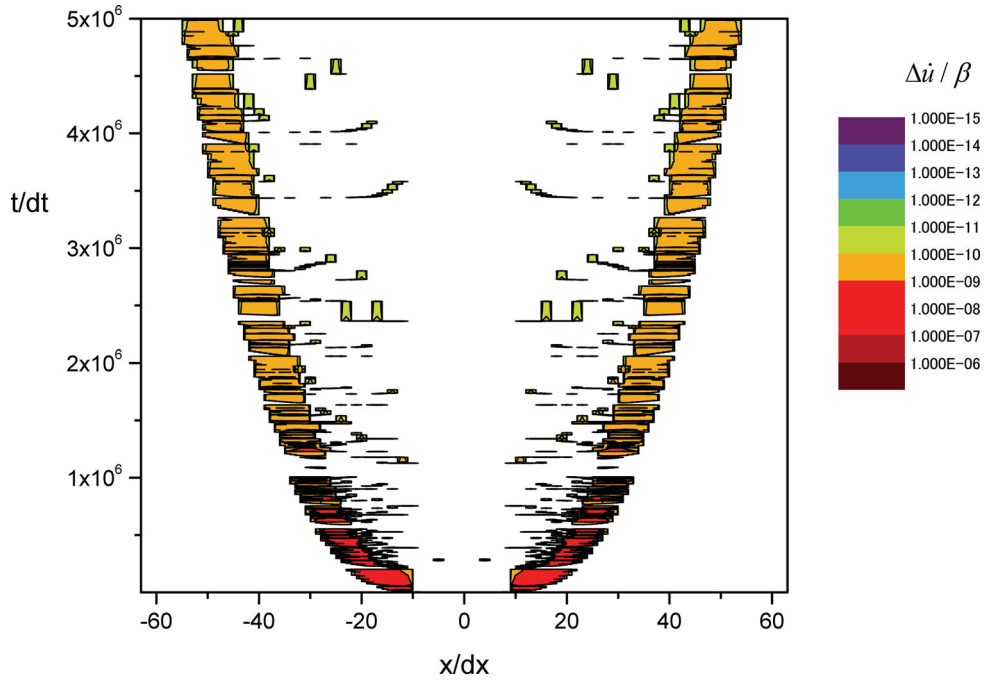

Figure 9. Spatiotemporal change of slip velocity during the rupture growth. Although we assume $\alpha_0 = 0.05$ and $k = 0.5 \times 10^{-11}$ m^2 in the same way as in Fig. 6, the damping coefficient c is set at 0 here. The slip velocity is plotted every 100 time steps as in Fig. 6.

the illustration of Fig. 12, we select out events that propagate 10 nodes or more and that occur after the rupture zone size exceeds four times the nucleation zone size. The effect of artificial fault nucleation is expected to be small enough for such rupture zone size. In addition, events having relatively long migration distance are required for reliable estimate of migration speeds. Although a limited number of reactivated slips are found to propagate with speeds close to the shear wave speed, such events are excluded in the illustration here. Fig. 12 indicates that the backward migration speed is roughly independent of node-interval size although it is not very conclusive because the number of calculated time steps is smaller for smaller values of dx. Fig. 12 also shows that backward migration speeds are much smaller than the shear wave speed and lie in a range from 10 km/h to 150 km/h. We also find a tendency that the backward migration speed decreases with the rupture growth. Larger speeds observed earlier in the sequence may be because

Downloaded from https://academic.oup.com/gji/article/193/1/375/742358 by guest on 23 April 2024

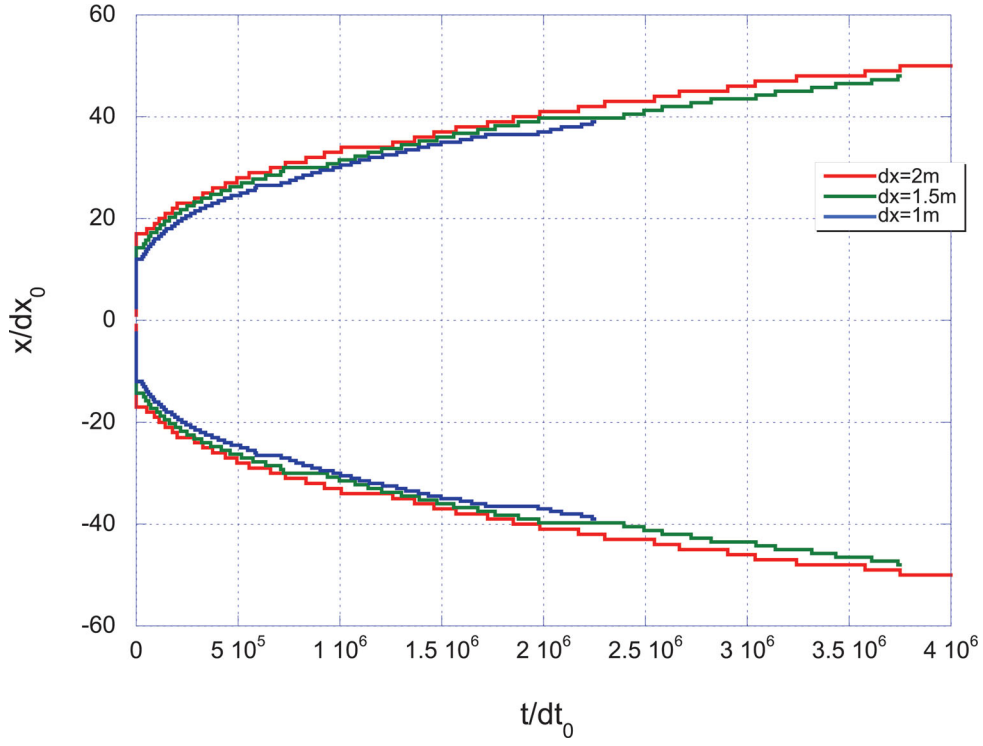

Figure 10. Effect of assumed sizes of node-interval and nucleation zone on the rupture growth; dx = 1, 1.5, 2 m are assumed. The values of permeability and slip-induced dilatancy rate are fixed at $k = 0.5 \times 10^{-11}$ m^2 and $\alpha_0 = 0.05$, respectively. The nucleation zone is located at $-n_i \mathrm{d}x \leq x \leq n_i \mathrm{d}x$ in all calculations here. Calculations are stopped earlier for smaller values of dx because of the capacity of computer. We also assume $\mathrm{d}x_0 = 2$ m and $\mathrm{d}t_0 = 4.193 \times 10^{-4}$ s ($=0.5\mathrm{d}x_0/\beta$) in the illustration.

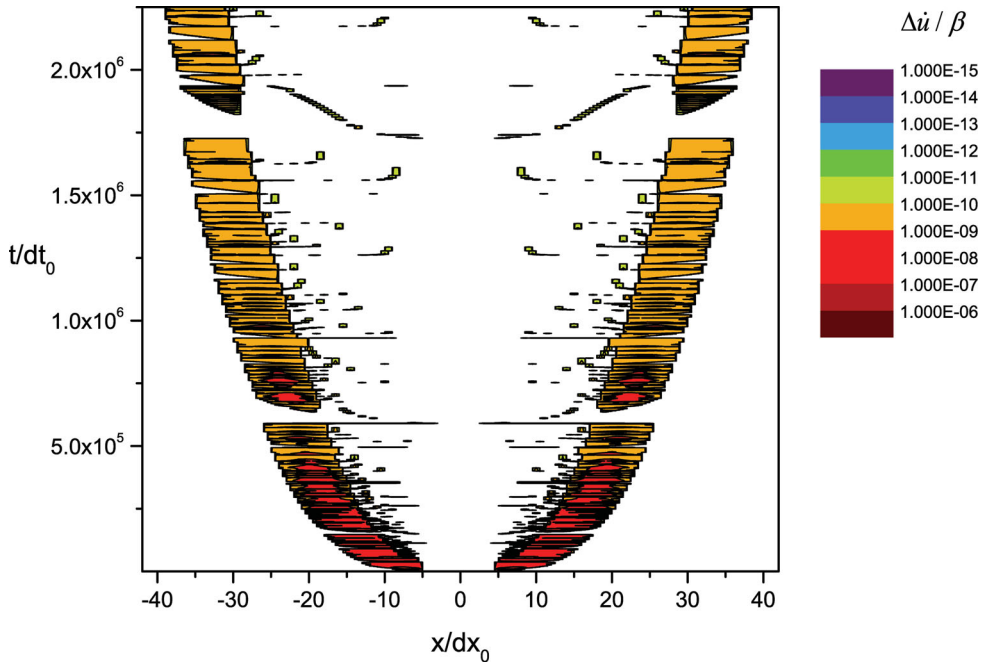

Figure 11. Spatiotemporal change of slip velocity during the rupture growth; the size of node-interval dx is fixed at 1m and the nucleation zone is located at $-10\mathrm{d}x \leq x \leq 10\mathrm{d}x$. We assume $k = 0.5 \times 10^{-11}$ m^2 and $\alpha_0 = 0.05$ in the calculation. Refer to the caption of Fig. 10 as to $\mathrm{d}x_0$ and $\mathrm{d}t_0$. The number of computed time steps is smaller than in Fig. 6 because larger computer memory is required in this case. The slip velocity is plotted every 100 time steps as in Fig. 6.

Downloaded from https://academic.oup.com/gji/article/193/1/375/742358 by guest on 23 April 2024

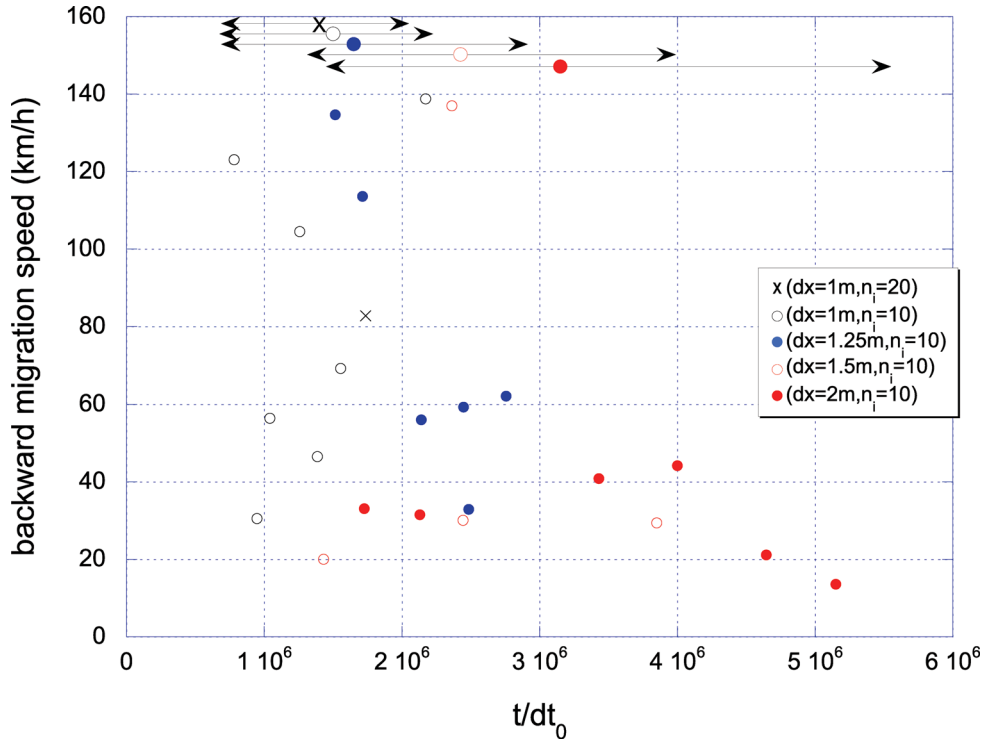

Figure 12. Dependence of backward migration speed of reactivated slip on the size of node interval and nucleation zone size; events with migration speeds close to the shear wave speed are excluded in this illustration. Refer to the caption of Fig. 10 as to dt_0. The number of calculated time steps is generally smaller for smaller values of dx because larger computer memory is required. Left right arrows with symbols denote the ranges of calculation for the assumed models. The values of permeability and slip-induced dilatancy rate are fixed at $k = 0.5 \times 10^{-11}$ m^2 and $\alpha_0 = 0.05$, respectively.

there still remains the effect of rupture nucleation. The simulated backward migration speeds are 10 to 60 km/h after the fault extends large enough distance, which is consistent with observations (Houston *et al.* 2011; Obara *et al.* 2012).

5.4 Mechanism of slow backward migration of reactivated slip

We now investigate the mechanism of slow backward migration of reactivated slip using an example illustrated in Fig. 7(a). We specifically investigate the slip reactivation in the time range $t/dt = 3.4338 \times 10^6$–$3.4341 \times 10^6$ for detailed analysis, which is magnified in Fig. 13; only the behaviour at $x < 0$ is shown because of the symmetry with respect to the origin $x = 0$. Fig. 13 shows that the nodal point at $x/dx = -40$ begins to slip at $t/dt = 3.433807 \times 10^6$ and small slip velocity is sustained there after the slip onset before the slip reactivation at the neighbouring nodal point $x/dx = -39$. Gradual increase in the fluid pressure will promote such sustained slip. In fact, Fig. 14 shows that gradual fluid pressure elevation occurs at $x/dx = -40$ soon after the sudden fluid pressure reduction at $t/dt = 3.433807 \times 10^6$. The sudden fluid pressure reduction is due to the pore creation accompanied by the slip; the gradual fluid pressure elevation will occur because of the fluid inflow from the neighbouring fault segments. At the nodal point $x/dx = -39$, the shear stress suddenly increases with the slip reactivation at $x/dx = -40$ and slowly increases with time mainly because of the sustained slip at $x/dx = -40$ (Fig. 15). Fig. 15 also shows that the failure strength at $x/dx = -39$ gradually decreases with time after some increase at the beginning. Such reduction of the failure strength is mainly due to the fluid pressure increase there; see also Fig. 14. Such changes in the fluid pressure and shear stress promote the slip reactivation at $x/dx = -39$. Similar behaviour is also observed at the segment $x/dx = -38$ after the slip reactivation at $x/dx = -39$.

5.5 Effects of α_0 and k on backward migration speeds of reactivated slips

Fig.16 illustrates the change of backward migration speeds of reactivated slips with rupture growth for some examples assumed in Fig. 1; the values of α_0 and k are fixed at 0.05 and 0.5×10^{-11} m^2 in Figs 16(a) and (b), respectively. In this illustration, events having migration speeds close to the shear wave speed are included. We find a conspicuous feature in Fig. 16 that there are no reactivation events whose backward migration speeds lie in a range between 50 m s^{-1}(= 180 km hr^{-1}) and 1000 m s^{-1}. Reactivated slips with backward migration speeds higher than 1000 m s^{-1} are now referred to as fast events; events with migration speeds lower than 50 m s^{-1} are referred to as slow events. Slow events can be a model for backward migration of tremors since the simulated backward migration speeds are roughly consistent with observations; Houston *et al.* (2011) and Obara *et al.* (2012) found migration speeds ranging from 1 to 60 km hr^{-1}.

We find a tendency in Fig. 16 that the ratio of number of slow events is larger for smaller values of permeability k and larger values of slip-induced dilatancy rate α_0. This will occur because larger values of k and smaller values of α_0 will elevate fluid pressure on the fault more rapidly; fault slip is accelerated more if the fluid pressure is higher on the fault. If we consider only slow events, we also find a tendency that backward migration speeds are lower for smaller values of permeability k and larger values of slip-induced dilatancy rate α_0. This means that backward migration speeds are lower when slow slip region extends with lower speeds: compare

Downloaded from https://academic.oup.com/gji/article/193/1/375/742358 by guest on 23 April 2024

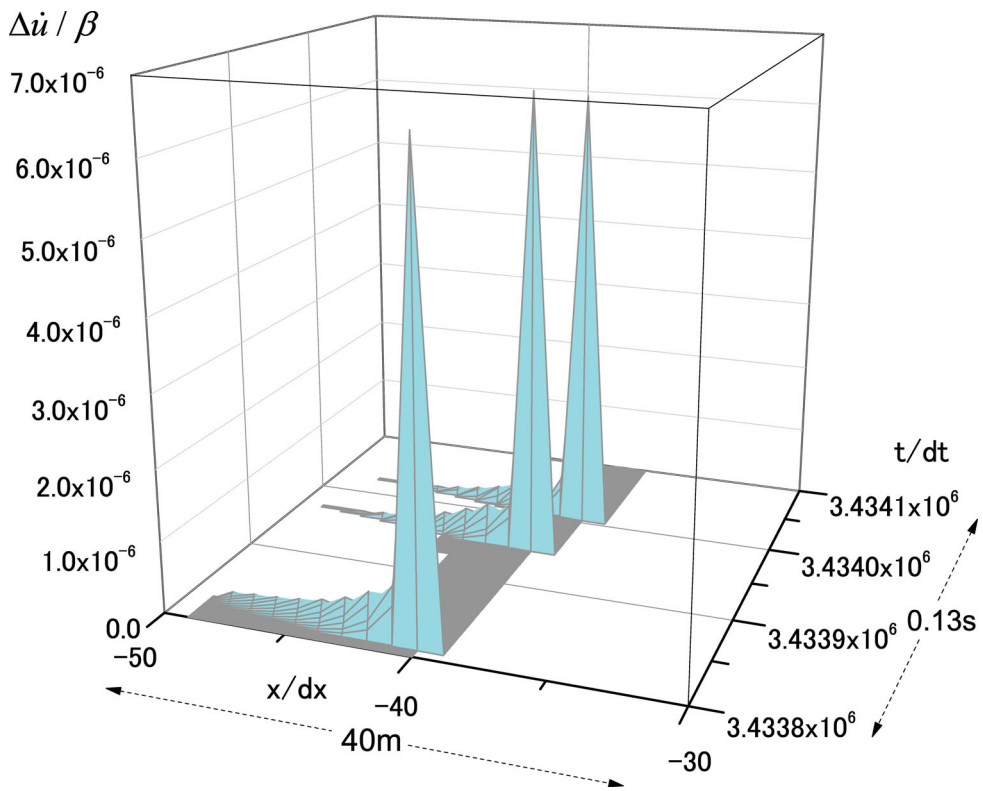

Figure 13. Close-up view of reactivated slip in the time range $3.4338 \times 10^6 < t/\mathrm{d}t < 3.4341 \times 10^6$ illustrated in Fig. 7a.

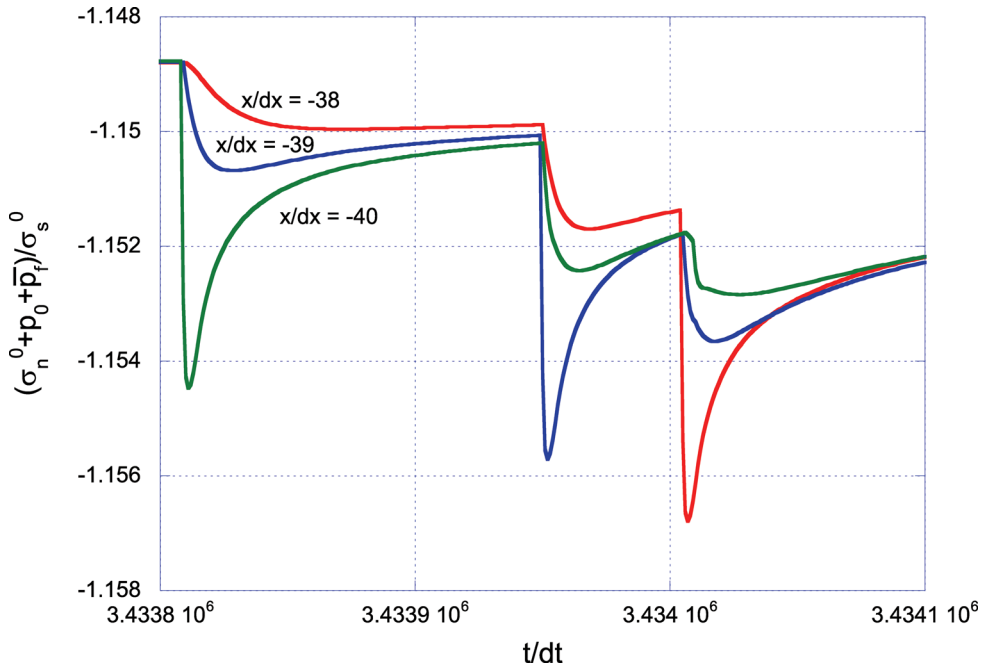

Figure 14. Temporal change of non-dimensional fluid pressure at the nodal points $x/\mathrm{d}x = -40$, -39 and -38 for the slip sequence shown in Fig. 13.

Fig. 1 with Fig. 16. Although the simulated backward migration speeds of reactivated slips are roughly consistent with observations, the assumed ranges of k and α_0 are not necessarily wide enough to reliably estimate these two values taken at zones of slow slip occurrence. In fact, it is difficult in the framework of our numerical computation to investigate the behaviour for $k \ll 0.5 \times 10^{-11}$ m^2 because rupture speeds are significantly low for such values of k; the rupture tips still lie at the nodal points $|x|/\mathrm{d}x = 36$ at time $t/\mathrm{d}t = 7.0 \times 10^6$ for $\alpha_0 = 0.05$ and $k = 0.1 \times 10^{-11}$ m^2. The rupture zone size attained at this time step is not much larger than the nucleation zone size. We cannot also make calculation for $k \gg 0.1 \times 10^{-10}$ m^2 because our method of numerical analysis becomes unstable for such large values of permeability.

Even if α_0 is large enough, we observe in Fig. 16(b) a small number of reactivation events propagating with speeds close to the shear wave speed. Although it is not very clear why such high-speed

Downloaded from https://academic.oup.com/gji/article/193/1/375/742358 by guest on 23 April 2024

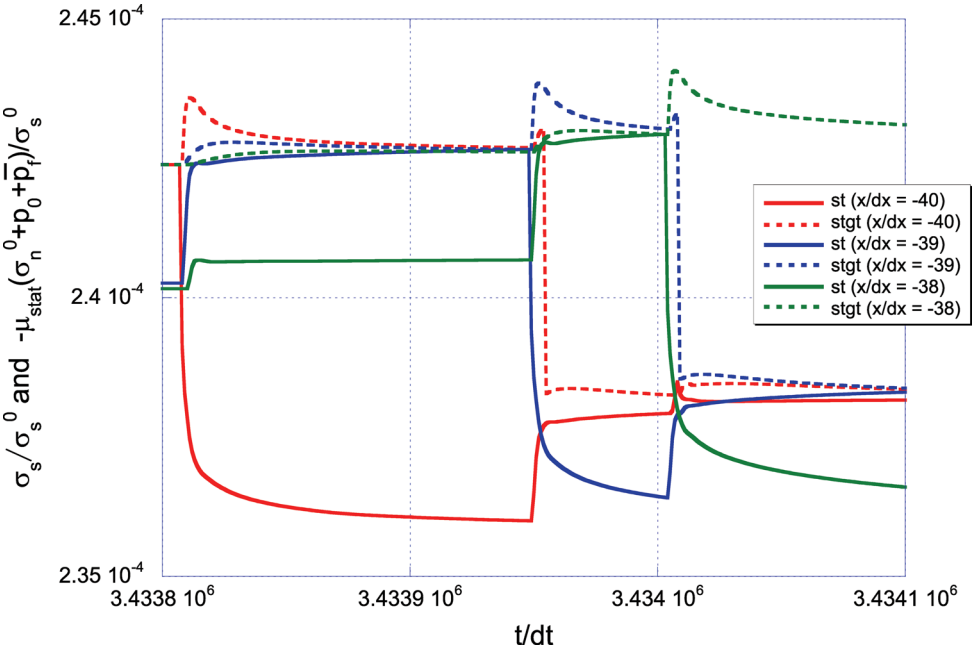

Figure 15. Temporal changes of non-dimensional failure strength (stgt $\equiv -\mu_{\rm stat}(\sigma_n^0 + p_0 + \bar{p}_{\rm f})/\sigma_{\rm s}^0$) and shear stress (st $\equiv \sigma_{\rm s}/\sigma_{\rm s}^0$) acting at the nodal points $x/{\rm d}x = -40$, -39 and -38 for the slip sequence illustrated in Fig. 13.

events are generated for such large values of α_0, it may be related to the spatiotemporal evolutions of fluid pressure and strength recovery. If the fluid pressure is higher and the strength recovery is smaller, we may observe higher propagation speed.

6 DISCUSSION

Our present study shows that we have to assume permeabilities larger than 10^{-12} m^2 for the simulation of slow slip coupled with tremor if fluid flow occurs only along a fault. These values are larger than supposed as permeabilities of exhumed faults (e.g. Faulkner & Rutter 2001; Wibberley & Shimamoto 2003) and of active subduction zones (e.g. Screaton *et al.* 2000; Bekins *et al.* 2011). For example, Wibberley & Shimamoto (2003) measured permeability of fault gouge of the Median Tectonic Line in Mie Prefecture, southwest Japan, and found fault rock permeabilities 10^{-21} to 10^{-13}m^2. Direct measurement by Bekins *et al.* (2011) on a shallow bore hole (∼500 m) that samples active fault zone at Barbados subduction zone shows permeabilities of 10^{-15} to 10^{-14} m^2. The fault gouge permeability was also measured in laboratory experiment with synthetic fault gouge by Zhang *et al.* (1999); they were in the range from 10^{-19} to 10^{-13} m^2. However, permeability of fault rocks is known to be larger for smaller effective stress (e.g. Rice 1992; David *et al.* 1994; Zhang *et al.* 1999). Since pore fluid pressure seems to be sufficiently high at zones of slow slips (e.g. Kato *et al.* 2010), we cannot rule out a possibility of permeabilities larger than 10^{-12} m^2. There is also a possibility that permeabilities are enhanced because of their transient variations associated with fault slip. For example, Miller *et al.* (2004) estimated fault zone permeability to be 4×10^{-11} m^2 by examining the migration of events in the 1997 Umbria-Marche earthquake sequence in central Italy. Noir *et al.* (1997) inferred a much larger fault zone permeability of 10^{-8} m^2 by studying the migration rate of events during the 1989 Dobi earthquake sequence in central Afar. In addition, if we consider dehydration reaction, we may be able to simulate higher pore fluid pressure than simulated in this paper (Brantut *et al.* 2010). Hence, we may be able to assume smaller permeabilities than assumed in this paper to simulate the slow slip and tremor observed in this paper. However, we have to note that the dehydration starting temperature should be close to the initial temperature for the occurrence of dehydration reaction because the temperature change is expected to be small enough in our model: shear heating is smaller for lower slip velocity.

Comparison between results obtained in YS11 and in this paper was one of our principal concerns. We compared the results in terms of the parameters α_0 and k in this paper. However, it is generally preferable to use non-dimensional parameters to understand the behaviour of physical phenomena. We actually examined the slip behaviour defining two non-dimensional parameters in YS11. We did not take such an approach here mainly because we cannot define the same non-dimensional parameters in the two studies. Note that although the two non-dimensional parameters defined in YS11 are functions of the shear zone thickness, the governing equation assumed in this paper is independent of it.

7 CONCLUSIONS

We studied in this paper how fluid flow along a fault affects the generation of slow slip and tremor, assuming dynamic modelling. Our study showed that the slip-induced dilatancy rate α_0 and permeability k play key roles in their generation. The calculation showed that rupture speeds consistent with observations of SSEs can be simulated in some ranges of α_0 and k. The rupture speeds were found to be lower for smaller values of k and for larger values of α_0. We found that fault slips stop soon after their onsets if the value of α_0 is large enough. Fluid flow along the fault can, however, reactivate frozen slips sporadically, and reactivated slips migrate backwards through a zone that has already ruptured. The calculations showed the existence of relatively slow backward migration speeds in a range 10–150 km hr^{-1}. We found a tendency that such backward migration speeds are lower for smaller permeabilitties and for larger slip-induced dilatancy rates. The above-mentioned

Downloaded from https://academic.oup.com/gji/article/193/1/375/742358 by guest on 23 April 2024

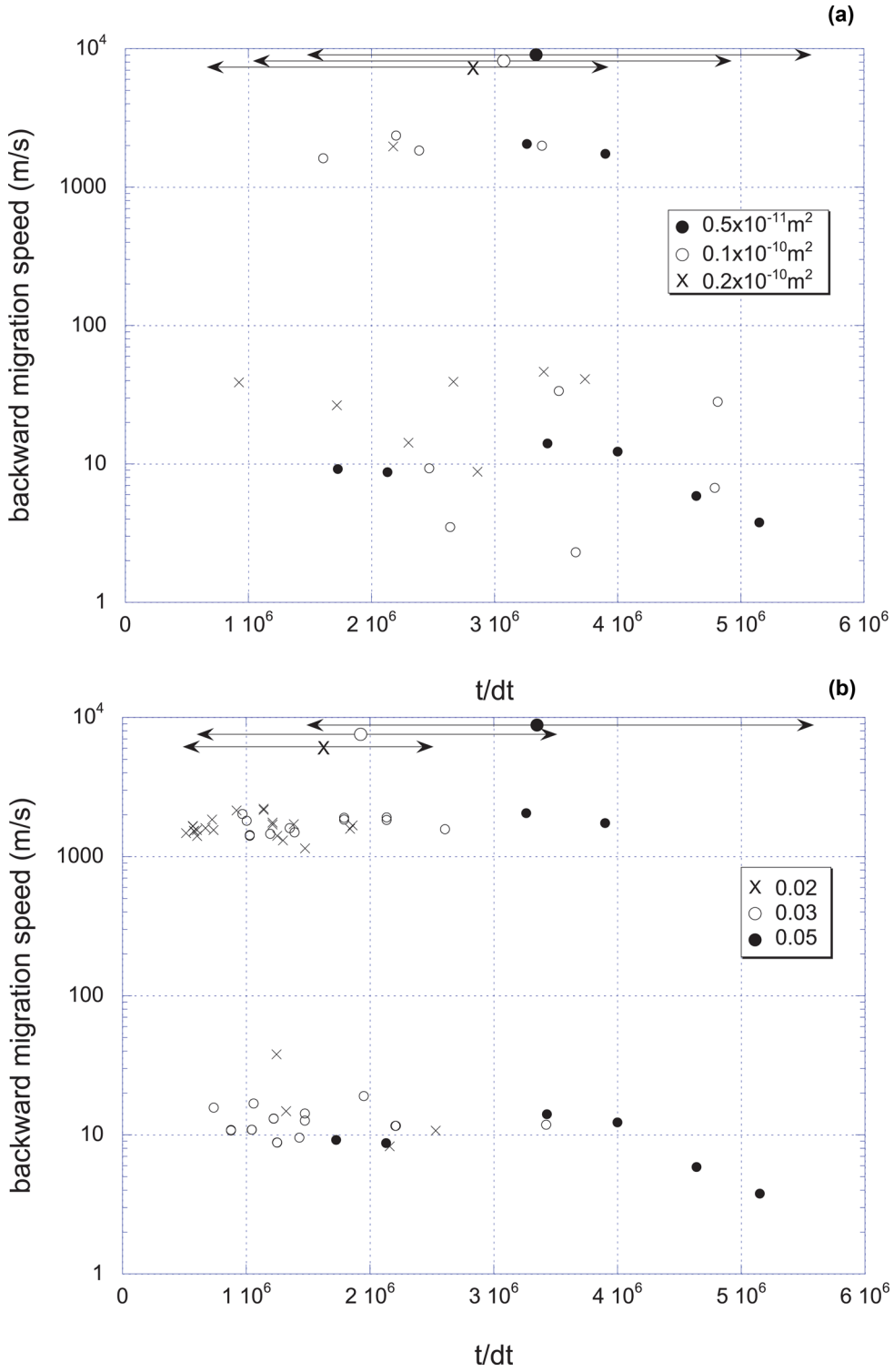

Figure 16. Change of backward migration speeds of reactivated slips with rupture growth for some examples illustrated in Fig. 1. The values of α_0 and k are fixed at 0.05 and 0.5×10^{-11} m^2 in (a) and (b), respectively. As in Fig. 12, we select out events that propagate 10 nodes or more and that occur after the fault size exceeds four times of nucleation zone size. Left right arrows with symbols denote the ranges of calculation for the assumed models. The calculation is stopped earlier for larger values of k and for smaller values of α_0 because such values of k and α_0 give rise to higher rupture speeds.

slip reactivations can be regarded as a model for tremor generation. Although a similar model was presented in YS11, a significant difference is that backward migration speeds of tremors simulated here are much more consistent with recent observations at Cascadia and southwest Japan.

Although the size of our model fault is much smaller than those of actual faults associated with slow slips, and assumed ranges of model parameters are not necessarily wide enough, our present study provides us with some insight into the generation mechanism of slow slip coupled with tremor.

Downloaded from https://academic.oup.com/gji/article/193/1/375/742358 by guest on 23 April 2024

ACKNOWLEDGMENTS

The author greatly appreciates helpful comments given by Y. Ben-Zion and two anonymous reviewers, which were quite useful to revise the manuscript.

REFERENCES

Andrews, D.J., 2004. Rupture models with dynamically determined breakdown displacement, *Bull. seism. Soc. Am.,* **94,** 769–775.

Ando, R., Takeda, N. & Yamashita, T., 2012. Propagation dynamics of seismic and aseismic slip governed by fault heterogeneity and Newtonian rheology, *J. geophys. Res.,* **117,** B11308, doi:10.1029/2012JB009532.

Bekins, B.A., Matmon, D., Screaton, E.J. & Brown, K.M., 2011. Reanalysis of in situ permeability measurements in the Barbados d´ecollement, *Geofluids,* **11,** 57–70.

Ben-Zion, Y., 2008. Collective behavior of earthquakes and faults: continuum-discrete transitions, progressive evolutionary changes, and different dynamic regimes, *Rev. Geophys.,* **46,** RG4006.

Ben-Zion, Y., 2012. Episodic tremor and slip on a frictional interface with critical zero weakening in elastic solid, *Geophys. J. Int.,* **189,** 1159–1168, doi:10.1111/j.1365-246X.2012.05422.x.

Byerlee, J.D., 1978. Friction of rocks, *Pure appl. Geophys.,* **116,** 615–626.

Colella, H.V., Dieterich, J.H., Richards-Dinger, K. & Rubin, A.M., 2012. Complex characteristics of slow slip events in subduction zones reproduced in multi-cycle simulations, *Geophys. Res. Lett.,* **39,** L20312, doi:10.1029/2012GL053276.

Brantut, N., Schubnel, A., Corvisier, J. & Sarout, J., 2010. Thermochemical pressurization of faults during coseismic slip, *J. geophys. Res.,* **115,** B05314, doi:10.1029/2009JB006533.

Canuto, C., Hussaini, M.Y., Quarteroni, A. & Zang, T.A., 2006. *Spectral Methods: Fundamentals in Single Domains,* Springer, Berlin.

Cochard, A. & Madariaga, R., 1994. Dynamic faulting under rate-dependent friction, *Pure appl. Geophys.,* **142,** 419–445.

Daub, E.G., Shelly, D.R., Guyer, R.A. & Johnson, P.A., 2011. Brittle and ductile friction and the physics of tectonic tremor, *Geophys. Res. Lett.,* **38,** L10301, doi:10.1029/2011GL046866.

David, C., Wong, T.-F., Zhu, W. & Zhang, J., 1994. Laboratory measurements of compaction-induced permeability change in porous rocks: implications for the generation and maintenance of pore pressure excess in the crust, *Pure appl. Geophys.,* **143,** 425–456.

Dieterich, J.H., 1972. Time-dependent friction in rocks, *J. geophys. Res.,* **77,** 3690–3697.

Dragert, H., Wang, K. & James, T.S., 2001. A silent slip event on the deeper Cascadia subduction interface, *Science,* **292,** 1525–1528.

Faulkner, D.R. & Rutter, E.H., 2001. Can the maintenance of overpressured fluids in large strike-slip fault zones explain their apparent weakness? *Geology,* **29,** 503–506.

Fukuyama, E. & Mikumo, T., 2007. Slip-weakening distance estimated at near-fault stations, *Geophys. Res. Lett.,* **34,** L09302, doi:10.1029/2006GL029023.

Hirose, H. & Obara, K., 2005. Repeating short- and long-term slow slip events with deep tremor activity around the Bungo channel region, southwest Japan, *Earth Planets Space,* **57,** 961–972.

Hirose, H. & Obara, K., 2006. Short-term slow slip and correlated tremor episodes in the Tokai region, central Japan, *Geophys. Res. Lett.,* **33,** L17311, doi:10.1029/2006GL026579.

Hirose, H. & Obara, K., 2010. Recurrence behavior of short-term slow slip and correlated non-volcanic tremor episodes in western Shikoku, southwest Japan, *J. geophys. Res.,* **115,** B00A21, doi:10.1029/2008JB006050.

Houston, H., Delbridge, B.G., Wech, A.G. & Creager, K.C., 2011. Rapid tremor reversals in Cascadia generated by a weakened plate interface, *Nat. Geosci.,* **4,** 404–409.

Ito, Y., Obara, K., Shiomi, K., Sekine, S. & Hirose, H., 2007. Slow earthquakes coincident with episodic tremors and slow slip events, *Science,* **315,** 503–506.

Kato, A. *et al.*, 2010. Variations of fluid pressure within the subducting oceanic crust and slow earthquakes, *Geophys. Res. Lett.,* **37,** L14310, doi:10.1029/2010GL043723.

Katsumata, A. & Kamiya, N., 2003. Low-frequency continuous tremor around the Moho discontinuity away from volcanoes in the southwest Japan, *Geophys. Res. Lett.,* **30,** 1020, doi:10.1029/2002GL015981.

Kostrov, B.V., 1964. Self-similar problems of propagation of shear cracks, *Appl. Math. Mech.,* **28,** 1077–1087.

Liu, Y. & Rice, J.R., 2005. Aseismic slip transients emerge spontaneously in three-dimensional rate and state modeling of subduction earthquake sequences, *J. geophys. Res.,* **110,** B08307, doi:10.1029/2004JB003424.

Liu, Y. & Rice, J.R., 2007. Spontaneous and triggered aseismic deformation transients in a subduction fault model, *J. geophys. Res.,* **112,** B09404, doi:10.1029/2007JB004930.

Liu, Y. & Rubin, A.M., 2010. Role of fault gouge dilatancy on aseismic deformation transients, *J. geophys. Res.,* **115,** B10414, doi:10.1029/20107JB007522.

Matsubara, M., Obara, K. & Kasahara, K., 2009. High-VP/VS zone accompanying nonvolcanic tremors and slow-slip events beneath southwestern Japan, *Tectonophysics,* **472,** 6–17.

Miller, S.A, Collettini, C., Chiaraluce, L., Cocco, M., Barchi, M. & Kaus, B.J.P., 2004. Aftershocks driven by a high-pressure CO_2 source at depth, *Nature,* **427,** 724–727.

Miyazawa, M. & Mori, J., 2005. Detection of triggered deep low-frequency events from the 2003 Tokachi-oki earthquake, *Geophys. Res. Lett.,* **32,** doi:10.1029/2005GL022539.

Noir, J., Jacques, E., Bekri, S., Adler, P.M., Tapponnier, P. & King, G.C.P., 1997. Fluid flow triggered migration of events in the 1989 Dobi earthquake sequence of Central Afar, *Geophys. Res. Lett.,* **24,** doi:10.1029/97GL02182.

Obara, K., 2002. Nonvolcanic deep tremor associated with subduction in southwest Japan, *Science,* **296,** 1679–1681.

Obara, K., 2010. Phenomenology of deep slow earthquake familyin southwest Japan: spatiotemporal characteristics and segmentation, *J. geophys. Res.,* **115,** B00A25, doi:10.1029/2008JB006048.

Obara, K., Hirose, H., Yamamizu, F. & Kasahara, K., 2004. Episodic slow slip events accompanied by non-volcanic tremors in southwest Japan subduction zone, *Geophys. Res. Lett.,* **31,** doi:10.1029/2004GL020848.

Obara, K., Matsuzawa, T., Tanaka, S. & Maeda, T., 2012. Depth-dependent mode of tremor migration beneath Kii peninsula, Nankai subduction zone, *Geophys. Res. Lett.,* **39,** L10308, doi:10.1029/2012GL051420.

Paterson, M.S. & Wong, T.-F., 2005. *Experimental Rock Deformation—The Brittle Field,* Springer, Berlin.

Rice, J.R., 1992. Fault stress states, pore pressure distributions, and the weakness of the San Andreas Fault, in *Fault Mechanics and Transport Properties of Rocks,* pp. 475–503, eds Evans, B. & Wong, T.-f., Academic, San Diego.

Rogers, G. & Dragert, H., 2003. Episodic tremor and slip on the Cascadia subduction zone: the chatter of silent slip, *Science,* **300,** 1942–1943.

Rubin, A.M., 2011. Designer friction laws for bimodal slow slip propagation speeds, *Geochem. Geophys. Geosyst.,* **12,** Q04007, doi:10.1029/2010GC003386.

Saffer, D.M. & Tobin, H.J., 2011. Hydrogeology and mechanics of subduction zone forearcs: fluid flow and pore pressure, *Ann. Rev. Earth planet. Sci.,* **39,** 157–186.

Schmidt, D.A. & Gao, H., 2010. Source parameters and time dependent slip distributions of slow slip events on the Cascadia subduction zone from 1998 to 2008, *J. geophys. Res.,* **115,** B00A18, doi:10.1029/2008JB006045.

Screaton, E., Carson, B., Davis, E. & Becker, K., 2000. Permeability of a decollement zone: results from a two-well experiment in the Barbados accretionary complex, *J. geophys. Res.,* **105,** 21 403–21 410.

Segall, P. & Rice, J.R., 1995. Dilatancy, compaction, and slip instability of a fluid-infiltrated fault, *J. geophys. Res.,* **100,** 22 155–22 171.

Segall, P., Rubin, A.M., Bradley, A.M. & Rice, J.R. 2010. Dilatant strengthening as a mechanism for slow slip events, *J. geophys. Res.,* **115,** B12305, doi:10.1029/2010JB007449.

Shelly, D.R., Beroza, G.C., Ide, S. & Nakamula, S., 2006. Low-frequency earthquakes in Shikoku, Japan, and their relationship to episodic tremor and slip, *Nature,* **442,** 188–191.

Shelly, D.R., Beroza, G.C. & Ide, S., 2007. Non-volcanic tremor and low-frequency earthquake swarms, *Nature,* **446,** 188–191.

Downloaded from https://academic.oup.com/gji/article/193/1/375/742358 by guest on 23 April 2024

Shibazaki, B. & Shimamoto, T., 2007. Modelling of short-interval slip events in deeper subduction interfaces considering the frictional properties at the unstable-stable transition regime, *Geophys. J. Int.,* **171,** 191–205.
Sleep, N.H., 1997. Application of a unified rate and state friction theory to the mechanics of fault zones with strain localization, *J. geophys. Res.,* **102,** 2875–2895.
Suzuki, T. & Yamashita, T., 2006. Non-linear thermo-poroelastic effects on dynamic earthquake ruptures, *J. geophys. Res.,* **111,** doi:10.1029/2005JB003810.
Suzuki, T. & Yamashita, T., 2007. Understanding of slip-weakening and slip-strengthening in a single framework of modeling and its seismological implications, *Geophys. Res. Lett.,* **34,** L13303, doi:10.1029/2007GL030260.
Suzuki, T. & Yamashita, T., 2008. Nonlinear effects of temperature, fluid pressure and inelastic porosity on dynamic fault slip and fault tip propagation: emergence of slip-strengthening and pulse-like fault slip, *J. geophys. Res.,* **113,** B07304, doi:10.1029/2008JB005581.
Suzuki, T. & Yamashita, T., 2009. Dynamic modeling of slow earthquakes based on thermoporoelastic effects and inelastic generation of pores, *J. Geophys. Res.,* **114,** B00A04, doi:10.1029/2008JB006042.
Suzuki, T. & Yamashita, T., 2010. Nondimensional control parameters governing the behavior of 1-D fault slip: effects of shear heating, inelastic pore creation and fluid flow, *J. geophys. Res.,* **115,** B02303, doi:10.1029/2009JB006557.
Tanaka, Y. *et al.*, 2010. Gravity changes observed between 2004 and 2009 near the Tokai slow-slip area and prospects for detecting fluid flow during future slow-slip events, *Earth, Planets Space,* **62,** 905–913.
Wech, A.G., Creager, K.C. & Melbourne, T.I., 2009. Seismic and geodetic constraints on Cascadia slow slip, *J. geophys. Res.,* **114,** B10316, doi:10.1029/2008JB006090.
Wibberley, A.J. & Shimamoto, T., 2003. Internal structure and permeability of major strike-slip fault zones: the Median Tectonic Line in Mie prefecture, southwest Japan, *J. Struct. Geol.,* **25,** 59–78.
Yamashita, T. & Fukuyama, E., 1996. Apparent critical slip displacement caused by the existence of a fault zone, *Geophys. J. Int.,* **125,** 459–472.
Yamashita, T., 1998. Simulation of seismicity due to fluid migration in a fault zone, *Geophys. J. Int.,* **132,** 674–686.
Yamashita, T., 1999. Pore creation due to fault slip in a fluid-permeated fault zone and its effect on seismicity: generation mechanism of earthquake swarm, *Pure appl. Geophys.,* **55,** 625–647.
Yamashita, T. & Suzuki, T., 2011. Dynamic modeling of slow slip coupled with tremor, *J. geophys. Res.,* **116,** B05301, doi:10.1029/2010JB008136.
Zhang, S., Tullis, T.E. & Scruggs, V.J., 1999. Permeability anisotropy and pressure dependency of permeability in experimentally sheared gouge materials, *J. Struct. Geology,* **21,** 795–806.

APPENDIX A: DISCRETIZATION OF EQ. (1)

We now discretize eq. (1) and use the Adams–Bashforth method in the calculation of time evolution of fluid pressure (e.g. Canuto *et al.* 2006, p. 520). We specifically employ the second-order Adams–Bashforth method, so that eq. (1) is reduced to

$$\bar{p}_f^{i+1,j} = \bar{p}_f^{i,j} + \frac{M}{2}\Delta t \left\{ 3\left[\left(\frac{k}{\eta}\frac{\partial^2 \bar{p}_f}{\partial x^2} \right)^{i,j} - \left(\frac{\partial \phi_{in}}{\partial t} \right)^{i,j} \right] - \left[\left(\frac{k}{\eta}\frac{\partial^2 \bar{p}_f}{\partial x^2} \right)^{i-1,j} - \left(\frac{\partial \phi_{in}}{\partial t} \right)^{i-1,j} \right] \right\}, \quad \text{(A1)}$$

where the superscripts i and j denote $t = i\mathrm{d}t$ and $x = j\mathrm{d}x$. If we assume higher order methods, calculations will be more accurate if the variation of fluid pressure change is sufficiently smooth. However, we should note that the fluid pressure changes abruptly at the onset of slip in our model as simulated in YS11. In such a case, the abrupt fluid pressure change may artificially be smoothed more by the use of higher-order methods. Hence, higher order methods will not necessarily give rise to more accurate results in our simulation. We replace the second spatial derivative by the second order finite difference

$$\nabla^2 \bar{p}_\mathrm{f} = \frac{\partial^2 \bar{p}_\mathrm{f}}{\partial x^2} \simeq \frac{\bar{p}_\mathrm{f}^{i,j+1} - 2\bar{p}_\mathrm{f}^{i,j} + \bar{p}_\mathrm{f}^{i,j-1}}{(\mathrm{d}x)^2} \quad . \quad \text{(A2)}$$

We assume $\bar{p}_\mathrm{f} = p_0$ over the plane $y = 0$ at $t = 0$.

APPENDIX B: EFFECTS OF NODE-INTERVAL SIZE AND NUCLEATION ZONE SIZE ON MACROSCOPIC RUPTURE BEHAVIOUR

We first examine how the assumed size of node interval affects macroscopic-scale rupture behaviour. We consider rupture propagation and moment evolution as examples of macroscopic-scale rupture behaviour (Figs B1 and B2). We assume two values $\mathrm{d}x = 1$ and 2 m as the size of node interval. Note that values of $\mathrm{d}t$ are smaller for smaller values of $\mathrm{d}x$ because of the relation $\beta \mathrm{d}t/\mathrm{d}x = 0.5$ assumed

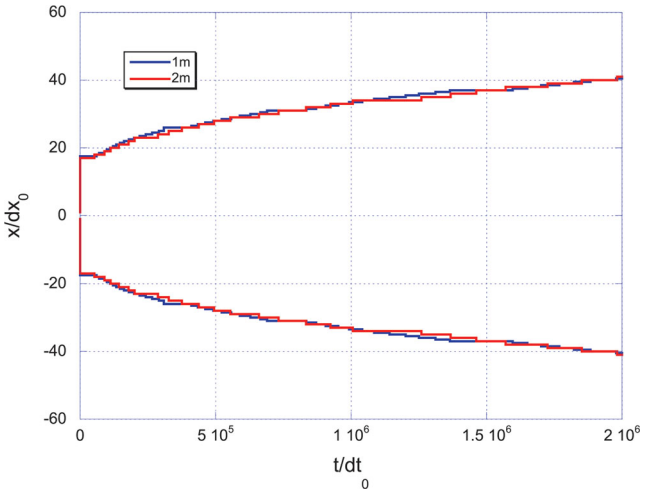

Figure B1. Effect of assumed size of node-interval on the rupture propagation; $\mathrm{d}x = 1$ and 2 m and are assumed in the calculation. We assume $k = 0.5 \times 10^{-11}$ m^2, $\alpha_0 = 0.05$ and the same nucleation zone size in both cases. We assume $\mathrm{d}x_0 = 2$ m and $\mathrm{d}t_0 = 4.193 \times 10^{-4}s(=0.5\mathrm{d}x_0/\beta)$ in the illustration. Irregular changes are due to slip reactivation.

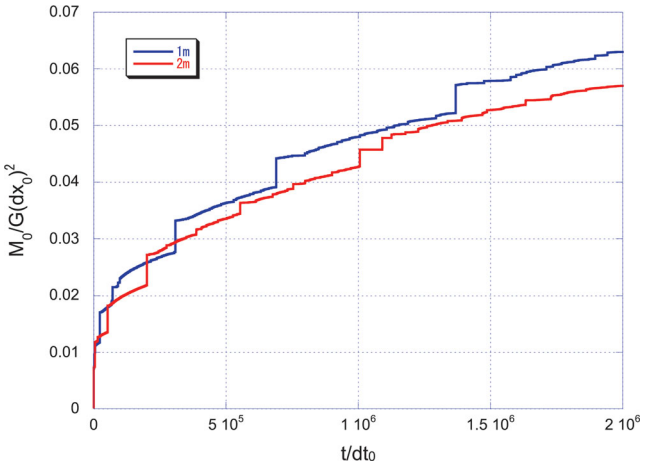

Figure B2. Effect of assumed size of node-interval on the moment evolution for the models assumed in Fig. B1. Irregular changes are due to slip reactivation as observed for the curve of rupture growth in Fig. B1. Refer to the caption of Fig. B1 as to $\mathrm{d}x_0$ and $\mathrm{d}t_0$.

Downloaded from https://academic.oup.com/gji/article/193/1/375/742358 by guest on 23 April 2024

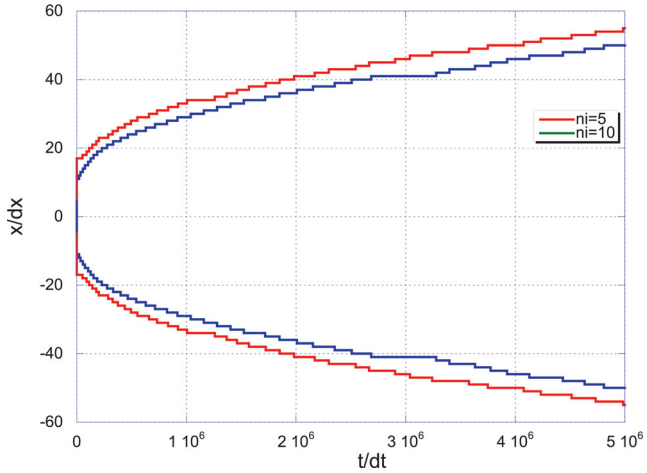

Figure B3. Effect of nucleation zone size on the rupture propagation; $n_i = 5$ and 10 are assumed and the value of dx is fixed at 2 m. We assume $k = 0.5 \times 10^{-11}$ m^2 and $\alpha_0 = 0.05$ in both cases.

in this paper. The nucleation zone size is fixed at 40m in all calculations here. We also assume $k = 0.5 \times 10^{-11}$m^2 and $\alpha_0 = 0.05$ here. Since we assume the slip-weakening at the onset of earliest slip at each location on the fault, we expect that macroscopic rupture behaviour is nearly independent of assumed size of node interval. Figs B1 and B2 actually show that this is the case. Slight discrepancy between the two cases occurs because of slip reactivation, which is regarded as mesoscopic rupture phenomenon in this paper (see Section 5).

We next examine the effect of nucleation zone size on the rupture propagation. We assume two values $n_i = 5$ and 10; the nucleation zone lies at $-n_i \mathrm{d}x \leq x \leq n_i \mathrm{d}x$ as mentioned in the text. The values of dx, k and α_0 are fixed at 2 m, 0.5×10^{-11}m^2 and 0.05, respectively, as assumed in many examples in this paper. Fig. B3 shows that the overall rupture speed is almost independent of the nucleation zone size when the rupture zone size is much larger than the nucleation zone size. Although not shown here, the moment evolution rate is also found to be almost independent of the nucleation zone size. It is not practical to assume much larger values for n_i because of the capacity of computer.

Downloaded from https://academic.oup.com/gji/article/193/1/375/742358 by guest on 23 April 2024